

DR. EUGENE C. RANKEY (Orcid ID : 0000-0002-1603-2934)

Article type : Original Manuscript

Chemical oceanographic influences on sediment accumulations of a carbonate ramp: Holocene Yucatan Shelf, Mexico

Eugene C. Rankey¹, Rodrigo Garza-Perez², and Hassan Eltom³

¹ *Kansas Interdisciplinary Carbonates Consortium, Department of Geology, University of Kansas, USA*

² *Unidad Multidisciplinaria de Docencia e Investigación Sisal, Facultad de Ciencias, Universidad Nacional Autónoma de México, Puerto de Abrigo S/N, Sisal, Hunucmá, Yucatán, C.P. 97355, Mexico*

³ *College of Petroleum Engineering & Geosciences, King Fahd University of Petroleum & Minerals, Dhahran, Saudi Arabia*

Short Title – Upwelling and sediment, Yucatan Shelf, Mexico

Keywords – Carbonate, carbonate ramp, geochemistry, Mexico, rare earth elements, sedimentology, Upwelling, Yucatan

ABSTRACT

Global controls on the oceanographic influences on the nature of carbonate factories are broadly understood. The details of the influences of changes in temperature and nutrients across individual carbonate shelves are less well constrained, however. This study explores

This article has been accepted for publication and undergone full peer review but has not been through the copyediting, typesetting, pagination and proofreading process, which may lead to differences between this version and the [Version of Record](#). Please cite this article as [doi: 10.1111/SED.12780](https://doi.org/10.1111/SED.12780)

This article is protected by copyright. All rights reserved

spatial and temporal variations in chemical oceanography along and across the Yucatan Shelf, a modern carbonate ramp, and how these factors relate to variable bottom character, sediment and sediment geochemistry. *In-situ* sensors and remote-sensing data indicate the sporadic presence of cool, upwelled water with low dissolved oxygen and elevated Chlorophyll-a. This current-driven, westward flow of upwelled water is most evident in a zone just offshore of the northern peninsular shoreline, but its influence wanes *ca* 75 km offshore and as the shore turns southward. The impacts of this water mass include a transitional photozoan–heterozoan assemblage with biosiliceous components, relict grains and common thin Holocene sediment accumulations nearshore; further offshore are corallgal reefs and expansive sand plains. Geochemical proxies of bulk sediment, including high $\delta^{18}\text{O}$ and elevated HREE/LREE (heavy rare-earth element/light rare-earth element) ratios near, and downcurrent of, the upwelling source, are interpreted to represent the signal of nearshore, westward movement of the cool and nutrient-rich, upwelled water. Collectively, these data emphasize how local processes such as upwelling and longshore transport can variably influence carbonate sediment accumulations and their geochemical signatures, both along and across individual shelves. These data and insights provide an analogue for the influences of spatial variability of water masses in the geological record, and for accurate interpretation of stratigraphic changes of sedimentary and geochemical proxy data in carbonate archives.

INTRODUCTION

Carbonate depositional systems include a broad range of carbonate-producing organisms (Lees, 1975; James 1997; Schlager, 2003). Recognition of a range of carbonate factories, including tropical, cool water and microbial, each with distinct biotic associations, stratal geometries, mineralogy and diagenesis, has led to an enhanced appreciation of how and why the very nature and distribution of carbonate facies varies considerably across the globe.

Studies on Quaternary and Recent systems have provided insights into the general, global-scale trends in controls on the nature of the carbonate factory (for example, as summarized in Michel *et al.*, 2019). In modern oceans, for example, heterozoan and biosiliceous facies are common in temperate or cold climate settings, and these represent the archetypal

cool water carbonates, *sensu* James (1997). Nonetheless, these types of deposits also can be found in tropical and subtropical areas in which upwelling brings cool, nutrient-rich water to shallow shelves, creating conditions favourable for these biotic associations (e.g. Gammon *et al.* 2000; Gammon & James 2001; Westphal *et al.*, 2010; Michel *et al.*, 2018, 2019).

At the scale of individual shelves, however, the influence of spatial and temporal variability in temperature and nutrients on carbonate systems remains poorly constrained. As a result, these parameters may be delimited inadequately in ancient analogues, and their impacts may be misunderstood by use of proxies.

In this context, this study examines how the sedimentological and geochemical character of shallow carbonate accumulations are impacted by upwelled waters. Specifically, given the general conditions of upwelling to the east and transport to the west across the nearshore parts of the shallow shelf, these waters might impact sediment across the shelf. Specifically, the cooler and nutrient-rich waters are expected to:

- *Influence carbonate-producing organisms.* The relative abundance of photozoan organisms, favoured in warm, oligotrophic, shallow water, would be subdued relative to the abundance of organisms of the heterozoan association, less influenced by nutrients and temperature.
- *Be reflected in the geochemical signatures of marine carbonates.* Sediment should include temperature and REE+Y signatures of upwelled water, such as higher $\delta^{18}\text{O}$ and greater HREE/LREE ratios, relative to areas less influenced by the upwelled water.
- *Vary spatially, along and across the shelf.* These upwelled-water influences would be most pronounced close to their source to the east and along their flow path west across the shelf than farther away, as they mix with normal-marine shallow water.

To explore these hypotheses, this study describes geomorphology, carbonate sedimentology, chemical oceanography and sediment geochemistry (rare earth elements and Yttrium – REE+Y – trace elements, and isotopes of oxygen and carbon) of the nearshore part of a modern carbonate ramp, offshore Yucatan Peninsula, Mexico. The actualistic study provides data that constrain and quantify the variable oceanographic conditions that impact the overall transitional heterozoan–photozoan association, as well as lateral changes in the nature of

carbonate accumulations and geochemical proxies on this modern shelf. The results provide a baseline for enhanced interpretation of oceanographic influences on spatial variability in deposition of ancient counterparts.

BACKGROUND

Study area

The Yucatan Shelf (also known as the Campeche Bank) extends north and west from the exposed karst plain of the Yucatan Peninsula, Mexico (Fig. 1). This shelf represents a subtropical distally steepened ramp, extending from the shoreline with gradients of *ca* 0.5 to 1.0 m/km (*ca* 0.03 to 0.06°) to the break in slope, which occurs in water depths of between 80 m and 280 m, at distances up to 300 km from the shoreline (Logan, 1969). This study focuses on areas within 30 km of shore, on the north-east, north-west, and west parts of the shelf (Fig. 1), regions with water depths generally less than 25 m. It expands on the descriptions of Lowery & Rankey (2017) from near Isla Arena to the south-west, and Neal (2020) from offshore Holbox to the east, with special focus from Sisal and Celestun, areas previously not documented in detail.

Along the north-eastern Yucatan Shelf, upwelling brings deep, cold (as low as 16°C), nutrient-rich water to the surface (Cochrane, 1966; Merino, 1997; Enriquez *et al.*, 2010). The shallow shelf is impacted by the Yucatan Current, a feature that originates near Holbox on the eastern flank of the Yucatan Shelf, then flows west. This current carries the upwelled water to the west along the northern Yucatan coast to Sisal, then less consistently to the south-west on the west-facing coast near Celestun and Isla Arena (Enriquez *et al.*, 2010).

Offshore waves dominantly are from the northeast, driven by trade winds, and offshore mean annual significant wave height (H_s) is roughly 2.5 m. Larger waves occur in association with passage of cold fronts, locally termed Nortes, and tropical depressions, and waves are smaller in summer when winds blow more gently. Smaller waves also occur on the western parts of the Yucatan Shelf in the Bay of Campeche, which represents the leeward protected side of the peninsula. As a result of these seasonal differences in wave conditions, the water column can become stratified, with a well-defined pycnocline in summer (even in nearshore areas <5

km from land; Enriquez *et al.*, 2013), but it is generally well-mixed in winter. Diurnal–semidiurnal mixed tides of the nearshore regions include small tidal range, from 0.1 m (neap tide) to 0.8 m (spring tide). These tides generate strong currents only locally, and are not a dominant control on regional water movement.

Precipitation varies seasonally. The mean precipitation in Celestun between 1982 and 2012 was 732 mm/yr, but ranges from averages of less than 10 mm in March and April to 144 mm in September. To the east, Cancun receives an average of 1400 mm/yr, with minimum average of 29 mm in April and maximum average of 282 mm in October. Precipitation from tropical depressions clearly exceeds these averages, however. Conversely, at times during the dry season, an entire month can pass without rain.

Recent studies of this modern tropical Yucatan shelf (Lowery & Rankey, 2017; Neal, 2020) revealed the occurrence of upper shoreface to lagoonal transitional heterozoan–photozoan carbonates. The sediment includes dominant bivalves and gastropods, foraminifera and barnacles, with locally abundant green algae (gravel-producing *Halimeda*, but also various mud-generating species). In contrast, corals, ooids and peloids are uncommon, and absent in most nearshore areas. Some areas include biosiliceous (diatom and sponge spicule) sediment, some of which is organic rich (in excess of 10% total organic carbon – TOC). A previous study (Lowery & Rankey, 2017) suggested that the nearshore heterozoan–photozoan assemblage and the biosiliceous sediment are favoured by the presence of the westward-moving, upwelled, nutrient-rich, cool water in this area.

Methods

This characterization of sediment and seafloor features expands on the observations from more than 500 points, including 242 sediment samples from seven transects offshore Isla Arena (Lowery & Rankey 2017) and 202 sediment samples from nine transects offshore Holbox (Neal, 2020). Additional samples, offshore Sisal (n = 60) and Celestun (n = 84), were collected in small plastic vials and capped at depth to retain fines, unless depth or wave conditions prevented free diving, in which case samples were acquired by a van Veen grab sampler. Sample locations

marked with a hand-held GPS (global positioning system) also included depth measurement by a digital depth sounder. Bottom observations made at the time of collection by either scuba or free diving included description of sedimentological and ecological attributes, physical sedimentary structures, presence, type and abundance of benthic organisms, and biological structures such as tracks, trails and burrows; these attributes collectively define different 'bottom types'. Samples were freeze dried in the laboratory, and grain size was analysed using an ATM Sonic Sifter (Advantech Manufacturing, Inc., New Berlin, Wisconsin, USA) at University of Kansas to sieve each sample. Over 250 thin sections from sediment of the field areas provided the basis for characterizing the types, sizes and character of sediment across the shelf.

Two oceanographic sensors, Aqua TROLL 600 multiparameter sondes (In-Situ Inc., Fort Collins, CO, USA), captured some of the chemical oceanographic variability that impacts the nearshore part of the shelf. One sensor collected data in water *ca* 7 m deep roughly 4.5 km offshore from Sisal (the nearshore sensor), with a second sensor simultaneously monitoring conditions in water *ca* 18 m deep *ca* 27 km offshore of Sisal. These sensors captured data on temperature, salinity, suspended sediment, and dissolved oxygen (DO) every 0.25 hours for a total of *ca* 67 days during parts of two seasons ('spring' – 12 April to 22 May 2018, and 'summer' – 29 May to 26 June 2018).

To characterize major and trace elements, including rare earth elements, 60 samples of *ca* 0.2 g from the four areas were prepared by crushing and homogenization. Samples were not of specific biota, rather representing bulk samples. This general approach may lead to variability in absolute measurements related to biotic fractionation (Elderfield *et al.*, 1981; Pattan *et al.*, 2005; Xiong *et al.*, 2012). Similarly, the homogenization may have included grains of different abundances, sediment of different ages, or grains that had been transported, such that they do not reflect ambient oceanographic conditions at the time and location of sampling. The homogenization ideally will capture the trends, and smooth out some of the inherent variability (Liu *et al.*, 2019); in fact, capturing the trends spatially is the essence of some of the motivation for this study, and the specific hypotheses it aimed to test, as explicitly articulated above. Given that there would be an invariant ratio of REE concentration among different components of the bulk sediments (Xiong *et al.*, 2012), and that these components have grossly

similar abundances among samples, biological fractionation would not change the general trend of REE concentrations in the homogenized samples. The data are the results; potential limitations of interpretations are considered and discussed below, however, in the context of individual metrics.

Samples were analysed by ALS Minerals Service (Vancouver, Canada) using X-ray fluorescence spectroscopy for major elements (precision is >0.01%), and inductively coupled plasma mass spectrometry (ICP-MS) for trace and rare earth elements (precision is >0.01 ppm). Analyses used the ME-MS89 Super Trace method, in which 0.2 g of sample are added to sodium peroxide flush, mixed, then fused in a zirconium crucible at 670°C. The cooled melt is dissolved in 30% HCl, then analysed by ICP-MS, and data corrected for spectral inter-element interferences. Oxides analysed for this study include: SiO₂, Al₂O₃, Fe₂O₃, CaO, MgO, Na₂O, K₂O, P₂O₅ and SrO. Elements included C and S, as well as Ba, Cs, Ga, Nb, Rb, Sr, Th, Tl, U, V, Y, Zr, As, Bi, Hg, Ni, Sb, Se, Te and Zn. Rare-earth element concentrations analysed for this study include: La, Ce, Pr, Nd, Sm, Eu, Gd, Tb, Dy, Ho, Er, Tm, Yb and Lu.

Rare-earth elements (REE) include the 15 elements from ⁵⁷La to ⁷¹Lu, but also are grouped with ³⁹Y due to similar physical properties; collectively, these elements are termed REE+Y. These ions are nearly all trivalent, but are fractionated in seawater by varying mineral-seawater partition coefficients. The fractionations reveal aspects of the nature and evolution of the seawater, as captured in the minerals that precipitate from it, here, carbonate sediment (Elderfield & Greaves, 1982; Elderfield 1988; German & Elderfield, 1990).

Because their absolute, natural abundances vary considerably, reported REE abundances commonly are normalized to PAAS (Post-Archean Australian Shale; McLennan, 1989). The REE concentrations reported herein are raw abundances normalized to PAAS, unless explicitly stated otherwise. Various REE+Y anomalies are calculated based on the methods previously proposed by Bau & Dulski (1996), Webb & Kamber (2000) and Lawrence *et al.* (2006), as described explicitly below.

Because fractionations are somewhat distinct among REEs, a common means to characterize distinctions is by use of various ratios or anomalies. One ratio, HREE/LREE, describes the abundance of heavy REE (\sum Ho-Lu) normalized to the abundance of light REE

(Σ La-Sm). Although LREEs are preferentially removed from solution in all seawater, advective transport plays an important role in deep-water masses (depths greater than 1 km; Elderfield, 1988; Zhang *et al.*, 2016). Because of distinct salinities and water mass history, various deep-water masses include notable differences in HREE/LREE ratios (e.g. Osborne *et al.*, 2017); of relevance here is that these deep-water ratios are almost always enriched in HREE relative to ratios from shallow(er) water masses, and thus include a greater HREE/LREE ratio. For example, surface Caribbean water include a mean ratio of *ca* 3.5, less than that found in deeper water (mean *ca* 4.3 at 1000 to 1500 m depth) (Osborne *et al.*, 2015).

Other ratios consider patterns of individual elements, or comparisons among a suite of elements, and can reflect distinct processes. For example, the Nd/Yb ratio has been used as another proxy for LREE and HREE differentiation. Modern seawater at depths of 50 m includes light ratios of shale-normalized data between 0.21 and 0.50 (de Baar *et al.*, 1985; Zhang & Nozaki, 1996), and higher values suggest LREE enrichment relative to this average marine signal. This ratio has been utilized to screen for altered seawater signals, with values greater than 1 interpreted to reflect the possibility of alteration from siliciclastic enrichment or other process. These causes commonly are tested by comparison with other proxies for contamination such as Al₂O₃ or SiO₂ abundances (Nothdurft *et al.* 2004).

The Ce/Ce* ratio is one metric that provides a means to characterize redox conditions. Relative to the other REE, Ce⁴⁺ is stabilized more readily under oxidizing conditions (Derry & Jacobsen, 1990; German & Elderfield 1990; Della Porta *et al.* 2015). Specifically, Ce anomalies can be calculated by comparing observed abundances with those expected of trivalent Ce³⁺, using the adjacent trivalent REE. For this study, the Cerium anomaly was calculated, following Lawrence *et al.* (2006), as $Ce/Ce^* = Ce/(Pr \times Pr/Nd)$. In this formulation, a negative Ce anomaly, or a value increasingly less than 1, suggests that Ce⁴⁺ is less abundant (for example, due to oxidation); reducing conditions are suggested by a positive anomaly, or Ce/Ce* increasingly more than 1. Of note, this formulation does not use Lanthanum in the calculation, so La enrichment would have no impact on calculated Ce/Ce* (Bau & Dulski, 1996; Lawrence *et al.*, 2006; Hueter *et al.*, 2019).

Similarly, this study follows Lawrence *et al.* (2006) and calculates the Lanthanum anomaly as $Pr/Pr^* = (0.5 * Ce + 0.5 * Nd)$. With this calculation, open-marine seawater REE signal includes values just greater than one, representing a slight positive La anomaly (De Baar *et al.*, 1991, Bau & Dulski, 1996).

Another measure, the Y/Ho ratio, has been interpreted to reflect the differences in complexation between the two elements, in that Y is scavenged by particles at one half the rate of Ho (Nozaki *et al.*, 1997). Modern seawater generally has a Y/Ho ratio of between 44 and 77, but varies regionally; for example, western Atlantic surface waters vary between 42 and 52 (Bau, 1996). This value is distinct from *ca* 25 for detrital siliciclastics (de Baar *et al.*, 1991; Bau, 1996; Bau & Dulski, 1996; Nozaki *et al.*, 1997), and *ca* 26 for freshwater (Lawrence *et al.*, 2006; Bolhar & Van Kranendonk, 2007; Zhao & Zheng, 2017).

The $\delta^{13}C$ and $\delta^{18}O$ of 40 inorganic carbonate samples were analysed at the Keck Paleoenvironmental and Environmental Stable Isotope Laboratory at the University of Kansas (KPESIL). Analysis included reaction of carbonate in anhydrous phosphoric acid at 73°C in a ThermoFisher Kiel IV Carbonate Device interfaced to the inlet of a ThermoFisher MAT 253 (ThermoFisher Scientific Inc., Waltham, MA, USA). The analysis was controlled by using six standards for each sample run. Consistency was enabled by use of two primary internationally recognized standards (NBS-18 and NBS 19) and four secondary standards (NIST SRM Dolomite 88b, Calcite X, TSF-1 and Sigma Calcite). The internal standards were calibrated through analysis at various laboratories and against NBS-18 and NBS-19 in KPESIL. Two standards were analysed at each step, at the beginning, the middle and the end of the run. Acid fractionation and temperature corrections are embedded in calibration to several international standards. The $\delta^{18}O$ and $\delta^{13}C$ data are reported in parts per mil (‰) relative to VPDB. The analytical precision for $\delta^{18}O$ and $\delta^{13}C$ isotopes is estimated to be better than $\pm 0.1\text{‰}$.

RESULTS

Geomorphology and sedimentology

The seascape, bottom types and sedimentology of the Isla Arena and Holbox lagoons and nearshore are described in detail elsewhere (Lowery & Rankey, 2017; Neal, 2020). As such,

they are only outlined here. Between these two areas lie Sisal and Celestun, where the peninsular shoreline orientation shifts from east-west to more north-south (Fig. 1). These areas are documented in detail and they are the focus of this study.

The shorelines of the northern and western peninsula include high-energy foreshore deposits of fine-medium sand (Holbox to Sisal) and bivalve coquina to mangrove (Celestun to Isla Arena). Westward to southward longshore drift has created protected lagoons behind the foreshore and beach ridges in several areas including Holbox, Celestun and Isla Arena (Lowery & Rankey, 2017; Neal, 2020).

On the north-facing coast, Holbox includes a foreshore of fine to medium sand. Nearshore regions (generally less than 10 m deep) include a nearshore subaqueous dune zone *ca* 2 km wide that passes further offshore to variable patches of bare sand, seagrass-covered sediment, and bedrock exposed at the seafloor. South of the barrier island of Holbox, a large (300 km²), shallow (<4 m) lagoon of mud-rich sediment is fringed by a mangrove marsh, but this lagoon is connected to the open ocean by a broad, shallow pass to the west. The samples analysed for geochemistry and described below represent only the subtidal, open-marine, upper shoreface and foreshore. No lagoon samples from the Holbox area are included.

Sisal, near the north-west corner of the Peninsula, includes a foreshore of fine to medium sand. The nearshore zone, extending up to roughly 10 km offshore and in water <10 m deep, includes a blanket of thin, discontinuous sand to gravel (Fig. 2A and B) covering a locally irregular rocky bottom. In these nearshore areas, fleshy brown algae, calcareous green algae (*Penicillus*, *Udotea* and some *Halimeda*; Fig. 2C) and minor seagrass patches occur, but they are not as abundant farther west, near Celestun and Isla Arena (see below). Small wave or current ripples are present, but not ubiquitous or persistent on sandy bottoms in this area. Areas greater than 10 km offshore (generally >10 m deep) include more patchy sediment, and in most areas rocky bottoms are evident (Fig. 2D), suggesting only thin sediment cover. Several kilometre-scale fields of roughly linear dunes occur in these water depths; and wave or current ripples are common. Areas with greater than 40 m of water depth (for example, more than 30 km offshore, beyond the study area) can include abundant wave ripples (Fig. 2E). During the

summer, abundant fleshy algae grows (Fig. 2F), and covers much of the seafloor, especially in the nearshore regions less than 30 to 40 km offshore.

Just west of Sisal, the shoreline turns more to the south-west, then to the south. This west-facing coast near Celestun and Isla Arena includes coarse bivalve coquina beach ridges prograding to the south, a dynamic that has created protected muddy lagoons (Lowery & Rankey, 2017). In these areas, within *ca* 10 km of shore (generally less than 10 m deep) bottoms are dominantly bare rippled to bioturbated sand (Fig. 3A), seagrass-stabilized sand and gravel (Fig. 3B), and *Halimeda* meadows (Fig. 3C). At distances more than 10 km offshore of Celestun, expansive sand plains (Fig. 3D) of complex, low-amplitude (mostly <1 m) bedforms are separated by patchy sediment covering a rocky bottom.

Given the subtropical latitude and absence of siliciclastics, the shallow shelf includes a notable paucity of corals, relative to Belize, the Caribbean coast of Mexico, or the Bahamas, for example. Corals present on some rocky substrates include *Solenastrea hyades* (Fig. 2F) *Cladocora* sp. and *Oculina* sp. (Fig. 3E), but do not appear to contribute much to the sediment, and sponges are evident across many areas (Fig. 3F). Several large coral reef complexes are evident further (>100 km) offshore, however, including Alacranes, Cayo Arenas, Cayo Arcas, Triangulos, Pera Bank and Nuevo Reef (Logan, 1969).

Bottom types (Fig. 4A and B), sediment size, sorting (Fig. 4C and D) and type (for example, Fig. 5A to F) vary across the area, and several large-scale trends are evident. First, grain size varies from foreshore to the upper shoreface. In general, the best sorted samples lie in nearshore subtidal bare sand areas within several hundred metres of shore (Fig. 5A and D). Fines are common <10 km of the shore, in water generally less than 10 m deep, near both Celestun and Isla Arena (Fig. 5A, B, D and E). In these areas, sediment can include up to 70% very fine sand and 16% mud (Fig. 4C and D). The protected lagoons of Celestun and Isla Arena are muddy as well but were not sampled systematically as part of this study (see Lowery & Rankey, 2017). More than 10 km offshore of both Celestun and Sisal, areas with water depths generally >10 m, all samples include less than 4% mud, but the abundance of the coarse fraction varies between the areas. Some samples 15 to 30 km offshore Sisal (the extent of this study; water depths can be 15 to 20 m or greater) include >50% coarse sand and gravel (Figs 4C and

5C); in contrast, off Celestun, the majority of samples beyond 15 km offshore are finer. These sediments, in water depths generally more than 10 m, include <25% coarse sand and gravel (Fig. 4D). In general, areas with subaqueous dunes tend to be moderately to well sorted fine to medium sand (for example, Fig. 5F).

Second, grain types are consistent with a transitional heterozoan–photozoan association; that is, most sediment producers are of heterozoans that tolerate cooler temperatures or elevated nutrients, with limited contributions from photozoans. The dominant grain types include skeletal fragments, molluscs (bivalves and gastropods) and foraminifera, along and across the shelf in the range of water depths. *Halimeda* is locally abundant near Celestun and Isla Arena in water less than 10 m, but much less common near Sisal; red algae, echinoderms and worm tubes are minor sediment contributors in all areas. Lithoclasts and micritized and bored ooids (Fig. 5B and C) occur in abundances of less than 5 to 10% in some samples offshore from both Sisal and Celestun; these are interpreted as relict (Logan 1969). Bivalves commonly are bored, and many other skeletal grains are partly to completely micritized and recognizable only by their shapes. Sponge spicules and diatoms are more common in the finer sediment to the west of the peninsula, and within the muddy lagoons (Lowery & Rankey 2017), but appear in samples scattered from across the shelf. No detrital silicate minerals (for example, quartz sand or silt) are noted across the shelf, at least the nearshore parts examined herein, consistent with the absence of fluvial or aeolian input across the peninsula, although some fine aeolian dust could be present (Li *et al.*, 2019).

These patterns are summarized in a map of the Sisal – Celestun region that indicates areas with distinct bottom types and sediment (Fig. 6). On this map, the fine sandy uppermost shoreface and bottoms covered with vegetation, including seagrass and calcareous algae, extend further offshore as the shoreline shifts to the south-west and then south. As noted above, however, vegetation is more abundant to the west. Similarly, a sandy-bottom region with linear barforms oriented roughly parallel to the shoreline extends across the area but broadens from 3 to 4 km wide offshore Sisal to about 10 to 15 km wide to the west. Outboard of this area, in water depths greater than 10 m, the region offshore Sisal is dominated by rocky bottom to thin sand and gravel deposits, with scattered fields of linear dunes. In marked contrast, the area

offshore of Celestun to the west includes complex dunes with moderately sorted, medium sand in roughly comparable water depths.

Chemical oceanography

Regional and seasonal trends

The chemical oceanography of the Gulf of Mexico varies at a range of space and timescales. Regional patterns of several oceanographic parameters, including salinity, sea-surface temperature (SST) and Chlorophyll-a, provide broad insights and a framework for understanding variability present across the study area.

Salinity is generally higher and shows greater seasonal variability in the shallower water of the shelf than in deeper, more fully open marine settings generally greater than 40 m water depth. Monthly average salinity during a representative winter month (November 2017) illustrates the occurrence of higher salinity (36.5 to 37.0 ppt) across the shelf than in much of the Gulf of Mexico or Caribbean (Fig. 7A). A plot of monthly average salinity for May 2018 illustrates similar salinity across much of the northern part of the shelf (north of the peninsula), but a general increase westward, into the Bay of Campeche (Fig. 7B), and towards the shoreline.

Sea-surface temperatures show spatial variability as well. Annual average SST are anomalously low within *ca* 50 km of the shoreline north of the Yucatan Peninsula, although they increase within a few kilometres of the shoreline (Enriquez *et al.*, 2013), areas of shallow water. For example, from Holbox to Celestun, areas within 75 to 100 km of the shoreline included mean annual SST in 2018 between 25°C and 26°C, several degrees cooler than surrounding waters. Monthly SST means for November 2017 (Fig. 7C) illustrate water across the shelf that is cooler than in the nearby Caribbean Sea. Nearshore and north of the peninsula, mean monthly sea-surface temperatures were 26 to 27.5°C. Likewise, average sea-surface temperatures for May 2018 were *ca* 25 to 26°C just north of the peninsula, the lowest sea-surface temperatures in the southern Gulf of Mexico and Caribbean, and cooler than the winter temperatures.

Like salinity and temperature data, Chlorophyll-a data document changes in space and time. Mean Chlorophyll-a during both November 2017 (Fig. 7E) and May 2018 (Fig. 7F) document progressive decreases from onshore to offshore. Notably higher monthly average

Chlorophyll-a, locally in excess of 30 mg/m³, occur nearer to the peninsular landmass, and during the winter months. Concentrations drop to less than 1.0 mg/m³ in the open Gulf of Mexico more than 100 km offshore.

In-Situ Sensor data: hourly changes nearshore and offshore

The monthly and annual averages reveal long-term seasonal shifts but smooth another level of temporal variability. To capture such variability, one sensor, a nearshore sensor, was posted 4.5 km away from the shoreline off of Sisal, and the other offshore sensor recorded conditions 27 km offshore of Sisal. These two sensors recorded data from 12 April to 27 June 2018 (Fig. 8) and illustrate a spectrum of changes related to individual atmospheric and oceanic events.

Spring. During the first, spring part of the deployment, a Norte dropped air temperatures from *ca* 30.5°C to *ca* 22.2°C around Days 3 to 4 (15 to 16 April 2018). This event was accompanied by: (i) decrease in temperature, more pronounced nearshore (Fig. 8A); (ii) decrease in salinity (Fig. 8C); (iii) relative increase in suspended solids, which was then followed by a decrease (Fig. 8E); and (v) decrease in dissolved oxygen (Fig. 8G). A second, less pronounced Norte passed around Day 16 (28 April 2018), with less marked impact, although suspended solids started to climb to *ca* 2 to 3 mg/l at both the nearshore and offshore sensors. A final weak Norte impacted the area around Days 25 to 27 (7 to 9 May 2018); following this event, temperature at the offshore sensor decreased from *ca* 26.5°C to less than 25°C (Fig. 8A), and temperatures remained below 25.5°C throughout June 2018. Concomitant with this offshore decrease in temperature was: (i) an increase in temperature at the nearshore sensor, such that daytime water temperatures even exceeded 29°C on two days (Fig. 8A); (ii) salinity offshore was maintained around 38 ppt (Fig. 8C); and (iii) suspended solids increased in excess of 50 mg/l (Fig. 8E). Throughout this deployment, dissolved oxygen remained above 7.0 mg/l, with the dissolved oxygen at the offshore sensor remaining roughly 1 mg/l higher than the nearshore sensor.

Early Summer. The later phase of the deployment, which constitutes early summer, illustrates patterns distinct from the previous deployment. For example, the lowest measured water temperature (23.7°C) occurred at the offshore sensor on Days 11 and 12 (9 and 10 June

2018) (Fig. 8B). In contrast, at the nearshore sensor, from an initial high, water temperature started to decline, and show less diurnal variability, on Day 12 (12 June 2018), reaching its lowest water temperature (27.3°C) on 20 June 2018. Salinity remained nearly constant at *ca* 36.8 ppt offshore, as during spring, but varied mostly between 38 and 39 ppt nearshore (Fig. 8D). At the nearshore sensor, suspended solids were below 1 mg/l from the start of the deployment until Days 11 and 12 (9 and 10 June 2018), when they increased to a maximum in excess of 300 mg/l on 12 June, followed by a decline to *ca* 10 to 100 mg/l, where they remained for the most part (Fig. 8F). In contrast, the offshore sensor remained below 2 mg/l until around Day 16 (14 June 2018), when they started to increase abruptly to more than *ca* 20 mg/l, where they remained until the end of deployment (Fig. 8F). On this deployment, on only three days did the dissolved oxygen exceed 7 mg/l nearshore; it likewise shows a general decline, remaining below 6 mg/l every day after Day 11 (9 June 2018). Offshore, dissolved oxygen measures showed a more pronounced decline, from a peak of 8.6 mg/l on Day 1 (29 May 2018) to 5.6 mg/l on Day 20 (18 June 2018). Similarly, as the offshore sensor DO levels dropped more precipitously than those at the nearshore sensor, the differences between the two converged from *ca* 1.5 mg/l difference at the start of the deployment to <0.5 mg/l different on Days 19 to 26, with DO lower offshore than nearshore during parts of four days (Fig. 8H).

High temporal resolution satellite data: daily changes across the shelf

The *in situ* observations, which include a wealth of detail on high-resolution temporal changes at two points, can be coupled with remote sensing data that document spatial variability at daily temporal resolution. Pairing optical, sea-surface temperature (SST) and Chlorophyll-a data (for example, Fig. 9) illustrate additional insights into the nature and controls on spatial and temporal variability of these chemical oceanographic parameters. Note, however, that the satellite records SST in the upper few micrometres of the ocean, whereas the sensors measure temperature at roughly 0.5 m above the seafloor.

For example, remote sensing data from 9 April 2018, a calm, clear spring day a few days before the deployment began (Fig. 9A to C) illustrate that near Sisal, warm (*ca* 28°C) water nearshore cooled to *ca* 26.5°C at locations *ca* 100 km offshore. Chlorophyll-a was above 1.0

mg/m³ near the shoreline on the north-facing coast near Sisal, but elevated Chlorophyll-a readings extended up to 50 km offshore on the west-facing coast south of Celestun. In contrast, following the Norte event of 15 to 16 April 2018, conditions changed markedly (Fig. 9D to F). Sea-surface temperatures are 26.5°C and below across the shelf (Fig. 9E), and Chlorophyll-a values in excess of 0.3 mg/m³ (mesotrophic of Hallock, 2001) reach several hundred kilometres offshore in eddies off the north-western part of the peninsula (Fig. 9F). These changes between 9 April and 18 April reflect relations among cooler atmospheric conditions, a well-mixed ocean, and sediment suspension, associated with passage of the Norte.

Another cool temperature event was recorded by the offshore sensor on 9 and 10 June 2018 (Day 12 of the second sensor deployment) (Fig. 9G to I). The satellite SST data reveal a body of cool water, as low as 25°C, extending from east of Holbox to west of Sisal (Fig. 9H). This cool water does not extend to the shoreline near Sisal and west or south-west, but stays offshore, and generally warms continuously to the west, the direction that the regional current flows. This body of water appears to persist, perhaps aided by a succession of cloudy days, with even cooler water, as low as 22°C, occurring near Holbox as of 22 June 2018 (Day 24) (Fig. 9J to L). These cooler waters are associated with elevated Chlorophyll-a concentrations in excess of 1 mg/m³ (eutrophic, per Hallock, 2001) offshore Sisal and Celestun, and had even reached hypertrophic conditions offshore of Holbox, with Chlorophyll-a in excess of 10 mg/m³ on 20 June 2018 (Fig. 9L). This time interval corresponds with periods of elevated sediment in suspension at the *in situ* meters, and the low and declining dissolved oxygen levels off Sisal.

To be clear, the timeframe of the sensor deployments, the focus of this data presentation, did not capture a full range of oceanographic variability. For example, conditions of 31 January 2019, a day considered fully winter, included turbid water with abundant sediment, elevated Chlorophyll-a, and cold water across the shelf (Fig. 8M to O).

Sediment geochemistry – major, trace, rare-earth element and isotope data

Major and trace element data

Major and trace elements document the dominance of carbonates in the samples. SiO₂ concentrations are all <1% (median 0.53%), except in the Isla Arena lagoon, where abundance

reaches up to 4.6%, and one sample just offshore of Sisal (1.27%) (Fig. 10A). Qualitative petrographic and scanning electron microscopy (SEM) observations suggest that the silica is dominantly biosiliceous, sourced from diatoms, radiolaria and sponges (Lowery & Rankey, 2017); no quartz sand or silt was evident in any thin section. Other trace elements that could document siliciclastic influences are low as well. For example, median Al_2O_3 abundance in the samples is 0.11% (Fig. 10B), with the highest abundance (0.49%) in the Isla Arena lagoon, and Thorium concentrations are all <0.6 ppm (Fig. 10C).

Rare earth element data

These data suggest that some samples include signatures not fully consistent with a signal from solely carbonate sediment. For example, some of the REE plots illustrated an irregular, or jagged, appearance. This appearance is related to limited precision, data near instrument detection limits, or both. Similarly, as discussed above, some samples include Al_2O_3 or SiO_2 concentrations that are elevated, and could reflect contamination by fine detrital influx or biosiliceous debris. Because the goal is to capture the seawater signal in carbonates, rather than artefacts from low concentrations or siliciclastic contamination, analyses reflect only those samples that include $<0.1\%$ Al_2O_3 , $<1.0\%$ SiO_2 and data at least four times the detection limits. These samples are referred to as 'pristine' in these sections.

The total REE concentrations (ΣREE) ranged from 0.30 to 0.85 ppm for the samples on the Yucatan Shelf (Table 1), and total abundances and abundances of individual elements show subtle distinctions within and among areas. The abundance of each REE for pristine samples are illustrated in plots from all areas (Fig. 10D). For example, the Holbox and Celestun samples generally are tightly clustered (for example, Fig. 10D), whereas the Sisal and Isla Arena samples are much more variable, and in general lower (Fig. 10D). Variability in samples includes onshore-offshore changes, as well, as discussed below. Mean REE distributions of pristine samples by each area (Fig. 10E) include broadly seawater-like trends.

The HREE/LREE ratios of Yucatan pristine samples include considerable spatial variability. For example, HREE/LREE ratios of Sisal samples show differences across the shoreface (Fig.

11A and B). Specifically, samples from more than 15 km of the Sisal shoreline include elevated HREE/LREE ratios (mean = 3.37). These areas also frequently include lower Chlorophyll-a (Fig. 11A) and lower SST (Fig. 11B). These elevated values are, however, quite distinct from ratios from samples within 15 km of the Sisal shoreline and across the Celestun shoreface (mean = 2.56), nearshore areas with elevated Chlorophyll-a and SST (Fig. 11A and B). In contrast, the HREE/LREE ratios of samples from near Holbox (mean = 3.58; Fig. 11C) are all greater than 3.0, and akin to those more than 15 km offshore Sisal.

Another metric used to compare relative abundances of light and heavy rare-earth elements is the Nd/Yb ratio. Considering all data, shale-normalized values range from 0.37 to 3.9, although 80% are less than 1.0. For all data, Nd/Yb is uncorrelated with $\sum\text{REE}$ ($R^2 = 0.03$); similarly, cleaning the data to include only samples more than four times the detection limits of Nd and Yb, and with less than 0.1% Al_2O_3 and <1.0% SiO_2 reveals no correlation with $\sum\text{REE}$ ($R^2 = 0.15$) (Fig. 12A).

In the Yucatan data, Ce/Ce* of all samples range from 0.36 to 1.11, and average 0.79, a negative anomaly. Considering only samples with low Al_2O_3 and measurements at least four times detection limits, spatial changes are evident at several scales. The Holbox samples (mean = 0.72) are the most consistently low Ce/Ce*, whereas Celestun samples include the highest mean Ce/Ce* (0.83); mean values near Sisal are intermediate (0.77). Ce/Ce* exceeds 0.9 in some samples within 15 km of shore near Sisal and up to 25 km offshore of Celestun (Fig. 11D); only one sample more than 15 km offshore of Sisal includes Ce/Ce* greater than 0.9. These anomalies can be compared with Ce/Ce* of Western Atlantic surface waters (WASW; samples from water depth <50 m), which range from 0.35 to 0.75 (average = 0.51) (van de Flierdt *et al.*, 2012; Osborne *et al.*, 2015), and with Bahamian ooids, which include Ce/Ce* between 0.75 and 0.87 (Li *et al.*, 2019).

The Pr/Pr* anomaly for pristine Yucatan samples (<0.1 % Al_2O_3 , <1.0% SiO_2 , and Ce, Nd and Pr at least four times greater than detection limits) ranges from 0.92, a slight negative anomaly, to 1.32, a positive anomaly. Mean Pr/Pr* is 1.1, reflecting a slight positive anomaly. Plotting Ce/Ce* versus Pr/Pr* (modified from Bau & Dulski 1996) for only pristine data reveals that the

majority of data include a negative Cerium anomaly and a positive Lanthanum anomaly (field IIIB of Bau & Dulski, 1996), although a handful include no anomaly (Fig 12B).

The mean Y/Ho ratio for the pristine Yucatan samples is 40.2 ($<0.1\%$ Al_2O_3 , $<1.0\%$ SiO_2 , and Y and Ho at least four times greater than detection limits). The data for individual samples ranges between 32 and 54, however. This mean and the range of data are on the low end of, but generally within the range of, carbonates interpreted as marine seawater values (cf. Tostevin *et al.*, 2016; Liu *et al.*, 2019). Y/Ho for all samples, and for these pristine samples, is uncorrelated ($R^2 < 0.10$) with Nd/Yb, or Al_2O_3 , Th and SiO_2 (for example, Fig. 12D to F).

Data on $\delta^{18}\text{O}$ and $\delta^{13}\text{C}$

Analysis of stable isotopes of oxygen and carbon from the same samples provides complimentary information (Fig. 13). The data include sediment from the foreshore up to 25 km offshore, and include nine samples from Holbox, 12 samples from Sisal, 10 samples from Celestun. The highest $\delta^{18}\text{O}$ values occur near Holbox. There, the mean $\delta^{18}\text{O}$ of -0.0% (range -1.0 to 0.3%) contrasts to mean $\delta^{18}\text{O}$ of -0.8% (range -1.6 to -0.5%) offshore of Sisal and -0.9% (range -1.6 to -0.2%) offshore of Celestun. Carbon stable isotopes show comparable differentiation. The lowest mean $\delta^{13}\text{C}$ values occur offshore Sisal (mean = 0.3% , range -1.5 to 2.1%); Celestun is intermediate (mean $\delta^{13}\text{C}$ = 0.8%), and maximum mean $\delta^{13}\text{C}$ (1.7%) occurs offshore Holbox (range 0.9 to 2.6%). Neither $\delta^{18}\text{O}$ nor $\delta^{13}\text{C}$ are correlated to water depth.

INTERPRETATION AND DISCUSSION

The geochemical data reflect oceanographic processes

The oceanographic monitoring and satellite data document the sporadic presence of cooler and nutrient-rich water, and the sediment character suggests that this ocean chemistry impacts the nature of the carbonate factory. Is there a geochemical signal of these upwelled waters? Assessing the reliability of geochemistry recording a depositional signal in carbonates requires evaluating the roles of siliciclastic contamination that could alter the primary oceanographic signal (Nothdurft *et al.*, 2004; Frimmel, 2009; Eltom *et al.*, 2017), scavenging by organic matter (Elderfield & Greaves, 1982; Elderfield *et al.*, 1990; Byrne & Lee, 1993; Della Porta *et al.*, 2015)

and diagenesis (Webb & Kamber, 2000; Nothdurft *et al.*, 2004; Azmy *et al.*, 2011; Hood *et al.*, 2018).

Siliciclastic contamination

A distinct factor that could influence the geochemical results would be the presence of siliciclastic detritus that could contaminate the carbonate signal. At a first pass, the absence of any river systems or siliciclastic longshore systems seems to minimize this likelihood. Similarly, silica-rich material in these samples is not considered to be coarse sediment, because petrographic observations document absence of detrital quartz or other siliciclastic silt or sand, and a dominance of biosiliceous contributions (cf. Lowery & Rankey, 2017).

The geochemical data furthermore are consistent with this interpretation in several ways. First, at the coarsest level, all but one of the shoreface samples were >99% carbonate, although several samples of the lagoon of Isla Arena included up to 5% SiO₂, largely as biosiliceous material.

Second, other potential indicators of siliciclastics are not present in abundance. For example, the Al₂O₃ abundance is low (0.1% in most samples) and mean Th abundance is less than 0.17 ppm (Fig. 10A to C), much less than the 0.6 ppm cut off above which siliciclastics have been interpreted to influence the geochemical signal (Webb & Kamber, 2000; Zhao & Zheng 2014, 2017).

Third, the low \sum REE, <0.9 ppm in all samples, also is broadly consistent with absence of a siliciclastic impact, which would tend to increase \sum REE. In all Yucatan data, lack of correlations between Al₂O₃ and \sum REE ($R^2 = 0.09$), or Al₂O₃ and HREE/LREE ($R^2 = 0.04$), suggest that such siliciclastic input is not a dominant factor in determining REE signals (Della Porta *et al.*, 2015; Liu *et al.*, 2019). Nonetheless, Liu *et al.* (2019) suggest that such low REE abundances can lead to inconsistent results, because any siliciclastic or clay portion that is present becomes (relatively) more important than the carbonate fraction that has low natural abundances.

Finally, the mean Y/Ho ratio is 40.2, a ratio lower than Western Atlantic seawater, although values for individual samples vary from 27 to 60. These data are within the range documented for other Holocene marine skeletal carbonates (e.g. Tostevin *et al.*, 2016; Lui *et al.*,

2019). Other proxies suggestive of siliciclastic contamination (for example, Al_2O_3) are not correlated to Y/Ho ($R^2 = 0.00$), however (Fig. 12D and E). Similarly, if detrital siliciclastics or biosiliceous material were an influence on Y/Ho, as their abundance increased, Y/Ho would decrease. Yet, the Yucatan data include no such trend (Fig. 12F), consistent with an interpretation of the absence of marked siliciclastic contamination (cf. Della Porta *et al.*, 2015).

A non-fluvial source of siliciclastics could be aeolian dust, as is known to occur in the Caribbean. Aeolian dust commonly is enriched in LREE relative to heavy minerals (e.g. Greaves *et al.*, 1999; Marx *et al.*, 2005; Hongo *et al.*, 2006; Tang *et al.*, 2013), because HREE-rich phases such as Zr are removed from the dust (Marx *et al.*, 2005). If LREE-enriched dust impacted these signals, it would be expected that the HREE/LREE and Nd/Yb ratios decrease (Della Porta *et al.*, 2015) in samples with increased siliciclastic contamination. None of these trends occur, however, in all data or pristine samples. For example, data for pristine samples illustrate R^2 of less than 0.22 for correlations between Nd/Yb and Al_2O_3 (0.07) SiO_2 , (0.01), or Th (0.22). Likewise, absence of correlation between Nd/Yb and ΣREE ($R^2 = 0.00$) or Nd/Yb and Y/Ho ($R^2 = 0.03$), is inconsistent with the trend expected if siliciclastic sediment impacted these REE signals (Fig. 12A and C) (cf. Saha *et al.*, 2019).

Nonetheless, although evidence suggests the lack of systematic siliciclastic influence among all samples, a subset of samples were separated and high-graded, as described above, and analysed separately (for example, Figs 10, 11 and 12A to C). These pristine samples form the basis for the interpretations below.

Particulate scavenging

Light REEs can be depleted in shallow seawater by the action of organic colloids or Fe-Mn oxyhydroxides, which remove LREEs from the water column, relative to HREEs. This process represents an important source of LREE depletion in shallow seawater (Elderfield & Greaves, 1982; Byrne & Kim, 1990; Elderfield *et al.*, 1990; Byrne & Lee, 1993; Sholkovitz *et al.*, 1994; Bau, 1996; Tachikawa *et al.*, 1999; Luo & Byrne, 2004).

If this process impacted the signal of Yucatan samples, it would be expected to have several related effects. It would increase the Y/Ho ratio, as particles preferentially scavenge Ho,

relative to Y (Byrne & Lee, 1993). The Y/Ho ratios in the Yucatan data that are lower than some marine waters and thus are not consistent with effects predicted by this scavenging process. Similarly, this scenario of scavenging control on the signal in these samples can be tested by comparing data with other expected results. For example, a second impact of scavenging would be an increase in ΣREE , while simultaneously decreasing LREE depletion (i.e. increasing the Nd/Yb ratio) (Della Porta *et al.*, 2015). Yet, the low ΣREE in the data are not consistent with this effect. If scavenging were a marked influence on REE patterns, however, it is expected that both lower Y/Ho ratios and elevated ΣREE are associated with increased Nd/Yb, that is, decreasing LREE depletion. As discussed above, ΣREE and Nd/Yb, and Y/Ho and Nd/Yb, both are uncorrelated ($R^2 = 0.12$ and 0.07 , respectively, for pristine data). Finally, scavenging would decrease the La anomaly as particles scavenge adjacent REE more than La (Sholkovitz *et al.*, 1994). As with the other scenarios, however, there is no correlation between La anomaly and Y/Ho ($R^2 = 0.00$ for all data, 0.06 for pristine samples). In summary, although several observations are not inconsistent with the possible effects of scavenging on the attributes of the Yucatan carbonate sediment, the bulk of evidence is interpreted to suggest the sediment in pristine samples is not impacted markedly by this process.

Freshwater input

Freshwater input could be another means to change the REE signal in these sediments, and could leave no SiO_2 or Al_2O_3 signal. Because freshwater includes dissolved REE abundances up to several orders of magnitude greater than seawater (Elderfeld *et al.* 1990), freshwater contributions of only 5 to 10% can markedly impact the REE patterns (Frimmel 2009; Bolhar *et al.* 2015; Zhao & Zheng, 2017). Freshwater tends to have a flat REE distribution, and Y/Ho of around 26 (Lawrence *et al.*, 2006).

This possibility is unlikely, for several different reasons. First, all of the regional oceanographic salinity data (Fig. 7A and B) indicate normal marine conditions across the shelf. Both the satellite data (Fig. 7A and B) and the sensor data (Fig. 8C and D) document greater salinity nearshore, where a freshwater influence by either springs or runoff would be most likely. It seems unlikely that a decrease in Y/Ho due to freshwater addition would not be

accompanied by a decrease in salinity at the sensors or in sea-surface data. Second, if freshwater additions modified the REE abundances, a positive correlation between ΣREE and Y/Ho, or HREE/LREE and Y/Ho might be expected. Neither is evident, with R^2 less than 0.1 for both. Thus, although groundwater flow from submarine springs or in restricted lagoons conceivably could be volumetrically sufficient to locally decrease Y/Ho of sediment in a local area, it is not interpreted to be a regional geochemical control.

Diagenesis

These samples all represent granular, unlithified sediment on the seafloor. As such, to a first approximation, they are unaltered by cementation, in the sense that they are neither cemented nor lithified. In detail, however, the presence of small lithoclasts (Fig. 5B) complicate a complete dismissal of the possibility of some cement signal. Although volumetrically uncommon (always less than *ca* 10% of the sediment, mostly less than 2%, and absent in many samples), small lithoclasts of cemented skeletal packstone to grainstone (possibly Pleistocene) and relict ooids are present, and could have been included in the REE and stable isotopic analyses. As a result, the possibility that these relict sediments record some cement in their geochemistry, a signal that could differ from ambient, present-day seawater, cannot be ruled out.

These samples may also include syndepositional diagenetic alteration, such as seafloor or shallow micritization, boring, or microbial activity. Many sediment grains are micritized and bored (Fig. 5E), suggesting that this possibility cannot be ruled out. On the other hand, this type of alteration would likely include alteration by seawater, and would not be markedly different than the seawater signal, unless they were buried for considerable time (Haley *et al.*, 2004). The thin, and mobile, accumulations on this shelf and the presence of relict ooids and lithoclasts suggest that the likelihood of persistent shallow burial is unlikely.

Variability in signatures.

The data show considerable variability. Several reasons might explain the ranges. First, the varied data could reflect sampling of a mix of sediment types (for example, bivalves,

foraminifera, *Halimeda* and echinoderms), because the sampling strategy did not isolate specific skeletal components for analysis. Several authors have suggested biotic differentiation of REE. For example, Webb & Kamber (2000) noted differences in average REE+Y patterns among corals, clams and coralline algal samples, and Akagi *et al.* (2004) noted fractionation even among four species of corals. These observed differences therefore could be due to biotic differentiation, as different organisms can incorporate REE into their skeletons with different partition coefficients. Alternatively, or additionally, mineralogical differences (for example, Mg-calcite of foraminifera and echinoderms versus aragonite of bivalves and *Halimeda*) could impact some ratios (cf. Scherer & Seitz, 1980; Webb & Kamber 2000).

Second, even if sediment types consistently record ambient seawater conditions, the specific skeletons that were sampled may have lived at different times. This temporal distinction could reflect seasonal growth, changing conditions at the seafloor, or both. A dense fleshy macroalgal canopy (Fig. 2F) grows during the dry season until the start of the Norte winds, when it collapses because of the increased wave action, the drop in temperature, and decreased sun incidence. Rapid growth of organisms (for example, *Halimeda*) may reflect the considerable seasonal organic matter decay associated with these changes; they thus could record conditions biased to reflect conditions during only one season, or even parts of one season (cf. Leonard *et al.*, 2019), rather than an alternate end-member seasonal or average annual state, as might be expected with slower-growing calcareous organisms such as bivalves or gastropods.

Another possibility is that the skeletons may be of different ages. Because the accumulation rates are low, surficial sediment could include organisms that died the year of sample collection, or those that passed several 1000 years ago. As such, it is possible that they accurately reflect conditions from that time, but oceanography that is distinct from those measured by sensors and satellites in 2017 to 2018.

Synthesis.

In summary, despite variable REE+Y distributions, and presence of some contaminated samples, several lines of evidence document that the pristine Yucatan samples preserve a seawater-like

shale-normalized REE pattern, including: mostly negative Ce/Ce* anomaly and positive Pr/Pr* anomaly; elevated Y/Ho ratio (average 40.2); LREE depletion (average Nd/Yb = 0.63); consistently positive Gd/Gd* anomalies (average = 1.18). Samples include lack of correlation between contaminant indicators and deviations in REE abundances or ratios that are predicted should there be widespread siliciclastic, aeolian silt or freshwater contamination. Although REE+Y occur in low abundance and variability is present, these results are interpreted to demonstrate the primacy of a seawater-related REE signal recorded in the pristine carbonate sediments.

Links among oceanography, bottom types, sedimentology and geochemistry

The bottom types, sediment and sedimentary geochemistry (trace elements, rare earth elements, oxygen and carbon stable isotopes) vary, both along and across this modern carbonate ramp shoreface system. Coupling the geological attributes (for example, sediment, bottom types and geochemistry) with controlling parameters (oceanography) provide a means to directly relate process with product.

Both the remote sensing data and the *in situ* monitoring document the spatial and temporal variability of chemical oceanographic influences across the nearshore parts of the Yucatan shelf. Specifically, regional data reveal that the nearshore shelf includes an average annual SST lower than those of the open Gulf of Mexico, and in the nearby Caribbean Sea (Fig. 7C). This dynamic is driven by cooler water that upwells to the east (near Holbox), and is driven alongshore to the west by the nearshore Yucatan current (for example, Fig. 9I and L), with greatest differentiation during the summer (Enriquez *et al.*, 2010, 2013). *In situ* sensors reveal that temperature at the seafloor decreases into the summer within the area of cooler water (Fig. 8A and B), perhaps associated with stratification. Lower, and more consistent, SST across the shelf are favoured during the winter (Fig. 9O), after the passage of Nortes, and in association with periods with extensive clouds (Fig. 9F).

These cooler water events also appear to be associated with elevated suspended solids and seasonally decreased dissolved oxygen (Fig. 8E to H). These patterns also are associated with elevated Chlorophyll-a (Fig. 9I, L and O). These relations suggest that the upwelled, cooler

water is nutrient-rich, and favours primary productivity, which in turn can decrease the dissolved oxygen, and lead to episodically dysoxic conditions, with DO < 5 mg/l.

These data demonstrate spatial variability in water attributes, along and across the shelf. The region can be divided into several bodies of water with distinct end-member characteristics, but with diffuse and temporally changing spatial boundaries (Fig. 14A). A first area (Zone 1) lies in water within 5 to 10 km of shore to the north of the peninsula, in water generally less than 10 m deep. This zone expands offshore to more than 25 km wide along the western peninsular coast, however, to water depths of up to *ca* 13 m. This zone includes highest and most variable temperature, with marked warming in summer. Relative to other areas, it has elevated and more variable salinity, elevated suspended sediment and Chlorophyll-a, and lower dissolved oxygen (Figs 7, 8, 9, 14B and 14C). These characteristics suggest the shallow waters are more impacted by evaporation and heating, as well as sediment suspension during Nortes, although some of this sediment in all likelihood reflects primary production. All of these factors would favour decreased DO, a phenomenon also reflected in the nearshore red tides that occur on this coast during summer (Enriquez *et al.*, 2010).

The second area (Zone 2) lies along the northern coast from offshore of Holbox to just west of Sisal, where it separates more broadly from the shoreline. It includes the cooler, upwelled water with lower, more constant salinity, and generally lower suspended solids. This zone includes cooler SST in the summer months than in winter or spring (Figs 8 and 14C), and intermediate Chlorophyll-a concentrations, with mean monthly Chlorophyll-a generally less than 2 mg/m³, less in the summer. This zone extends from *ca* 100 km offshore near Holbox to *ca* 75 km offshore of Sisal, but the boundaries are vague and temporally variable (for example, Fig. 9).

The third zone (Zone 3), not sampled in detail here, lies >75 km offshore of the peninsular north coast and represents the region not markedly impacted by the upwelled waters. These generally deeper (>40 m) water areas are essentially the same as those of the open Gulf of Mexico, with low Chlorophyll-a and generally consistent SST near 27.5°C (Fig. 14B and C). A final, fourth zone (Zone 4) lies more than 75 km offshore of the western peninsular coastline. This region includes waters very similar to those of Zone 3, but that are slightly

saltier, warmer and with slightly more Chlorophyll-a (Fig. 14B and C). These attributes are interpreted to reflect the subtle restriction within the Bay of Campeche.

The bottom type, sediment attributes, and geochemistry appear to be related to these water mass dynamics. Specifically, Zone 1 includes bare sand, most notably nearshore along the north-facing shoreline near Sisal (Fig. 4), or within 2 to 5 km of the Celestun and Isla Arena shoreline. Offshore of Celestun and Isla Arena, as the shoreline turns to the south, the abundance of seagrass-dominated and calcareous algae-dominated bottom increases considerably (cf. Fig. 4) within 10 to 15 km of the shore, passing outboard to an extensive field of subaqueous dunes of medium sand in water depths greater than *ca* 20 to 25 m. These areas, with elevated salinity and temperature, lower dissolved oxygen, and high Chlorophyll-a, include a lower HREE/LREE ratio (Fig. 11A and B) than Zone 2. Although numerous samples in this nearshore area off Sisal contain elevated Al₂O₃ or SiO₂, the pristine samples also include a less pronounced negative Ce anomaly (Fig. 11C), consistent with the less consistently well-oxygenated setting. This signature perhaps is related to seasonal episodic water-column dysoxia (for example, Fig. 8H) directly related to passage of upwelled, nutrient-rich water. Alternatively, and perhaps more likely, less oxygenated conditions could represent : (i) growth of algae and zooplankton; (ii) death of these biota; and (iii) subsequent bacterial degradation. The net impact on seafloor and shallow-burial pore-water conditions could be oxygen depletion, and these pore waters could impact the Ce/Ce* signal of sediment. Although not a direct impact of anoxia or dysoxia of upwelled waters within the water column, this chain of factors also would be favoured by the passage of nutrient-rich water.

In contrast, Zone 2 includes abundant rocky seafloor, thin sand to gravel accumulation, and linear dunes with scattered lithoclasts and relict ooids within sediment of a transitional heterozoan–photozoan association, such as present offshore of Sisal and near Holbox. The higher $\delta^{18}\text{O}$ in this zone near Holbox and offshore of Sisal, relative to nearshore Sisal, and all Celestun and Isla Arena, is consistent with the presence of these cooler waters. Similarly, the elevated HREE/LREE in this zone (Fig. 11A to C) is expected, because it may reflect upwelling of the deep-water Caribbean water that includes higher ratios (Osborne *et al.*, 2015). The negative

Ce anomalies, lower than in Zone 1 (Fig 11D), are broadly consistent with a more oxygenated setting in either the water column (cf. Fig. 8G and H) or in shallow-burial pore waters.

The sediments of Zones 3 and 4 were not examined systematically as part of this study, but observations suggest the common occurrence of expansive sand bodies ornamented with abundant wave ripples, in addition to some rocky outcrops, both of which can occur at depths greater than 40 m (Logan, 1969; Garza-Perez *et al.*, 2017). The occurrence of coralgall reef complexes such as Alacranes and Cayo Arcas banks in Zones 3 and 4 document normal-marine, oligotrophic conditions in those regions (Fig. 14B and C), and decreased influence of upwelled water.

At a larger scale, the paucity of typical Caribbean reef-building corals in the nearshore areas, the ubiquitous foraminifera and molluscs, and the locally common *Halimeda* in the nearshore areas are consistent with a transitional heterozoan–photozoan association (cf. James, 1997; Lowery & Rankey, 2017; Neal, 2020). The common rocky bottom and thin sediment accumulations, most notable in Zone 2, coupled with the presence of lithoclasts, relict ooids and bioeroded grains, are all consistent with slow rates of accumulation. These features and low accumulation rates would be expected with a faunal association with a marked heterozoan contribution (James 1997; Schlager, 2005), although clearly, waves and currents move sediment on this shelf.

STRATIGRAPHIC IMPLICATIONS

Since the initial recognition of distinct faunal associations in carbonates of different settings (e.g. Lees & Buller, 1972; Lees 1975), numerous studies have recognized carbonates that are different from the ‘classic’ Florida-Bahamas tropical, warm-water conceptual model (e.g. Illing, 1954; Ginsburg 1956; Purdy 1963; Ball, 1967; Shinn *et al.*, 1969; Rankey & Reeder, 2010). These associations, variably referred to as heterozoan or cool (to temperate) water carbonates (for example, summarized by James, 1997; Lukasik *et al.*, 2000; Mutti & Hallock, 2003; Schlager, 2005; Michel *et al.*, 2018), now have been recognized and described from modern and ancient settings.

Many geological studies emphasize variability in faunal associations and sedimentary REE+Y geochemistry documented through vertical stratigraphic patterns, and interpret these changes to represent oceanographic changes through time. In many, or perhaps even most, situations in which a depositional signal can be isolated, such an approach is appropriate and reveals regional and even global dynamics (e.g. Bellanca *et al.*, 1997; Zhou & Zheng, 2017; Li *et al.*, 2017; Hueter *et al.*, 2019; Liu *et al.*, 2019).

It is not inconceivable, however, that some ancient shelves are characterized by lateral changes in oceanographic parameters such as SST, Chlorophyll-a and dissolved oxygen, akin to those on the Yucatan Shelf. These lateral changes could in turn impact the biota and the REE+Y and trace element signatures that they contain, as in the Yucatan data. In this scenario, the spatial variability in water mass character, rather than – or in addition to – regional or global changes through time, could impact the stratigraphic record preserved in vertical stratigraphic sections.

For example, it is common in the stratigraphic record that ramps prograde and some even evolve into rimmed shelves (Wilson, 1975; Read, 1985; Wright & Burchette, 1998). Under such a scenario, the ultimate record of a shelf like the Yucatan would record aggradation and progradation through geological time. Consideration of such stratigraphic evolution of a system like this shelf may provide insights into patterns that could be reflected in the stratigraphic record.

In this overly simplistic exercise considering stratigraphic dynamics of a conceptual system, progradation of the shoreface as a whole would result in accumulation of an upward-shallowing succession across the shelf. A representative vertical section might include lower shoreface (LSF) deposits overlain by upper shoreface (USF) accumulations, and then foreshore (FS), berm, and perhaps palustrine deposits (Fig. 15). The upward grain association trends would reflect a change from photozoan in the deeper-water LSF with conditions like Zone 3, to transitional heterozoan–photozoan fauna in the more proximal, shallower USF with setting like Zone 2 and the FS of Zone 1. These changes would be accompanied by REE trends that could include a less pronounced Ce anomaly upward, from deposits of waters like those of Zone 3, to Zone 2, to Zone 1. Similarly, these changes would be accompanied by an upward increase in

HREE/LREE ratio (LSF to USF, Zone 3 to Zone 2), followed by a decrease (USF to FS, Zone 2 to Zone 1).

Similar oceanographic variability along-strike, from the northern shelf offshore of Sisal to the western, leeward shelf offshore of Celestun, could generate a distinct set of patterns. In the simple progradational scenario outlined above, the pattern would transition from a normal marine, oligotrophic LSF to a muddier, more nutrient-rich USF with a transitional heterozoan-photozoan association. This transition could include absence of the zone of elevated HREE/LREE, perhaps with upward increase in Ce/Ce*, although the latter is not unambiguously demonstrated in the pristine samples from Yucatan.

These sorts of vertical trends could be interpreted reasonably to reflect changes through time, based on geochemical and sedimentological attributes. The succession could reflect a change in water mass properties across the depositional basin, from subtropical, normal-marine, oligotrophic conditions to a more nutrient-rich and cooler regime.

These interpretations would be correct, in that the physical and chemical character of the water mass at the core or outcrop location indeed would have changed during accumulation of the succession. However, these dynamics do not necessarily reflect temporal changes in oceanography across the basin. Instead, changes may be driven by distinct water masses that variably impact the different parts of the shelf, and simple stratigraphic evolution; basin-scale oceanic setting and processes may remain unchanged.

Variations in sediment facies or REE recorded in the stratigraphic record may have been controlled by comparable water mass dynamics in the past. Only with detailed three-dimensional facies, sedimentological, and geochemical study would such impacts be discernible, however.

SUMMARY AND CONCLUSIONS

To provide a basis for interpretation of controls on sedimentation on ancient ramps, this study explores how the character of carbonate deposits is influenced by geomorphological setting and chemical oceanographic parameters on the Holocene ramp offshore of the Yucatan Peninsula, Mexico. Results reveal that sediment size, type and sorting vary across the area, as a function of

energy level and *in situ* production, but several large-scale trends are evident: (i) grain associations indicate a transitional heterozoan–photozoan association. Molluscs and foraminifera are the dominant sediment type, with locally common *Halimeda*. Corals are rare, peloids are generally absent. Small lithoclasts and relict ooids occur infrequently offshore of Sisal and Celestun; (ii) fines (<125 µm) are more common nearshore Celestun and Isla Arena, and in lagoons; areas with dunes tend to be better sorted; and (iii) thin sediment cover and rocky bottoms are common offshore of Sisal and Holbox.

Sensors deployed offshore of Sisal from April through to June 2018 captured chemical oceanographic variability, trends that are consistent with regional MODIS satellite data: (i) salinity increased (by up to 1.5 ppt) and was more variable nearshore; (ii) temperature was less variable and decreased (up to 5°C) offshore and into the summer; (iii) dissolved oxygen (DO) was lower nearshore and into the summer, reaching less than 5 mg/l at times; and (iv) suspended sediment increased during the passage of cold fronts and in association with the recorded lower temperature/lower dissolved oxygen (DO) periods.

Westward movement of cooler, upwelled waters nearshore is reflected in spatial (both along-strike and onshore–offshore) changes in sediment geochemistry. Specifically, oxygen stable isotopes decrease, and HREE/LREE ratios decrease, as waters flow along-strike away from the source. Additionally, although the data are less unambiguous, positive Ce/Ce* anomalies are more common in areas with elevated nutrients and chlorophyll (nearshore Sisal, Celestun, and Isla Arena), in regions with lower measured DO.

Collectively, these data and interpretations provide a conceptual model for relations among sediment, chemical oceanography, and sediment rare-earth element (REE) geochemistry on the modern ramp system. These results emphasize the role of along-strike movement of upwelled waters in the upper shoreface, influencing the carbonate factory several 100 km away from the deep-water source. Similarly, in terms of interpretation of the ancient, the results illustrate potential challenges on use of the nature of the carbonate factory and REE+Y geochemical metrics to interpret basin-scale or global-scale changes in chemical oceanography.

ACKNOWLEDGEMENTS

We acknowledge the Donors of the American Chemical Society Petroleum Research Fund for partial support of this research, to the sponsors of the Kansas Interdisciplinary Carbonates Consortium (KICC) for partially supporting this study. As this study built from the M.S. theses of Tom Neal and Jennifer Lowery, we are grateful to them for their assistance in the field for sample collection and for their analyses. Reviewers Irene Cornacchia, Adrian Immenhauser, Julien Michel, Gregory Webb, Anonymous, and Editor Giovanna Della Porta provided numerous constructive suggestions and perspectives that enhanced the paper and its presentation, and to them we extend our sincere appreciation.

DATA AVAILABILITY STATEMENT

The data that support the findings of this study are available from the corresponding author upon reasonable request.

Accepted Article

REFERENCES

- Akagi, T., Hashimoto, Y., Fu, F.-F., Tsuno, H., Tao, H. and Nakano, Y. (2004) Variation of the distribution coefficients of area earth elements in modern coral-lattices: species and site dependencies. *Geochim. Cosmochim. Acta*, 68, 2265–2273.
- Azmy, K., Brand U., Sylvester, P., Gleeson, S. A., Logan, A. and Bitner, M. A. (2011) Biogenic and abiogenic low-Mg calcite (bLMC and aLMC): Evaluation of seawater-REE composition, water masses and carbonate diagenesis. *Chem. Geol.*, 280:180–190.
- Ball, M. M. (1967) Carbonate sand bodies of Florida and the Bahamas. *J. Sed. Petrol.*, 37, 556-591.
- Bau, M. and Dulski, P. (1996) Distribution of yttrium and rare earth elements in the Penge and Kuruman iron-formation, Transvaal Supergroup, South Africa. *Precamb. Res.*, 79, 37–55.
- Bau, M., 1996. Controls on the fractionation of isovalent trace elements in magmatic and aqueous systems: evidence from Y/Ho, Zr/Hf, and lanthanide tetrad effect. *Contr. Min. Petr.*, 123, 323-333.
- Bellanca, A., Masetti, D., and Neri, R. (1997) Rare earth elements in limestone/marlstone couplets from the Albian-Cenomanian Cismon section (Venetian region, northern Italy): Assessing REE sensitivity to environmental changes. *Chem. Geol.*, 141, 141-152.
- Bolhar, R., and Van Kranendonk, M.J. (2007) A non-marine depositional setting for the northern Fortescue Group, Pilbara Craton, inferred from trace element geochemistry of stromatolitic carbonates. *Precam. Res.*, 155, 229-250.
- Bolhar, R., Hofmann, A., Siahi, M., Feng, Y., and Delvigne, C. (2015) A trace element and Pb isotopic investigation into the provenance and deposition of stromatolitic carbonates, ironstones and associated shales of the ~3.0 Ga Pongola Supergroup, Kaapvaal Craton. *Geochim. Cosmochim. Acta*, 158, 57-78.
- Byrne, R.H., and Kim, K.-H., (1990) Rare earth element scavenging in seawater. *Geochim. Cosmochim. Acta* 54, 2645–2656.
- Byrne, R.H., and Lee, J.H. (1993) Comparative yttrium and rare earth element chemistries in seawater. *Mar. Chem.* 44, 121–130.

- Cochrane, J.D. (1966) The Yucatan current, upwelling off Northeastern Yucatan, and currents and waters of Western Equatorial Atlantic. *Oceanography of the Gulf of Mexico*. Progress Report TAMU Ref. no. 66-23T, p. 14-32.
- de Baar, H., Schijf, J., and Byrne, R. (1991) Solution chemistry of the rare earth elements in seawater. *Eur. J. Solid State Inorg. Chem*, 28, 357-373.
- de Baar, H.J.W., Bacon, M.P., and Brewer, P.G. (1985) Rare earth elements in the Pacific and Atlantic Oceans. *Geochim. Cosmochim. Acta*, 49, 1943-1959.
- Derry, L.A., and Jacobsen, S.B. (1990) The chemical evolution of Precambrian seawater: evidence from REEs in banded iron formations. *Geochim. Cosmochim. Acta* 54, 2965–2977.
- Della Porta, G., Webb, G.E., and McDonald, I. (2015) REE patterns of microbial carbonate and cements from Sinemurian (Lower Jurassic) siliceous sponge mounds (Djebel Bou Dahar, High Atlas, Morocco). *Chem. Geol.*, 400, 65-86.
- Elderfield, H. (1988) The oceanic chemistry of the rare-earth elements. *Philos. Trans. R. Soc. London A*, 325, 105– 126.
- Elderfield, H., and Greaves, M. J. (1982) The rare earth elements in sea water. *Nature*, 296, 214–219.
- Elderfield, H., Hawkesworth, C.J., Greaves, M.J., and Calver, S.E. (1981) Rare earth element geochemistry of oceanic ferromanganese nodules and associated sediments. *Geochim. Cosmochim. Acta*, 68, 45, p. 513-528
- Eltom, H., Abdullatif, O., and Makkawi, M.H. (2017) Rare earth element geochemistry of shallow carbonate outcropping strata in Saudi Arabia: Application for depositional environments prediction. *Sediment. Geol.*, 347, 51-68.
- Enriquez, C., Marino-Tapia, I.J., and Herrera-Silveira, J.A. (2010) Dispersion in the Yucatan coastal zone: implications for red tide events. *Cont. Shelf Res.* 30, 127–137.
- Enriquez, C., Marino-Tapa, I., Jeronimo, G., and Capurro-Filigrasso, L. (2013) Thermohaline processes in a tropical coastal zone. *Cont. Shelf Res.* 69, 101-109.
- Frimmel, H.E. (2009) Trace element distribution in Neoproterozoic carbonates as palaeoenvironmental indicator. *Chem. Geol.*, 258, 338–353.

- Gammon, P.R., James, N.P., and Pisera, A. (2000) Eocene spiculites and spongolites in southwestern Australia: not deep, not polar, but shallow and warm. *Geology*, 28, 855-858.
- Gammon, P.R., and James, N.P. (2001) Palaeogeographical influence on Late Eocene biosiliceous sponge-rich sedimentation, southern Western Australia. *Sedimentol.*, 48, 559-584.
- Garza-Perez, J.R., Rankey, E.C., Rodriguez-Vázquez, R. A., and Naranjo-Garcia, M. J. (2017) Satellite derived seafloor bathymetry and habitat mapping on a shallow carbonate platform: Campeche Bank, México. American Geophysical Union, Fall Meeting 2017, abstract #OS22B-05.
- German, C.R. and Elderfield, H. (1990) Application of the Ce anomaly as a paleoredox indicator: the ground rules. *Paleoceanography*, 5, 823-833.
- Ginsburg, R.N. (1956) Environmental relationships of grain size and constituent particles in some South Florida carbonate sediments. *AAPG Bull.*, 40, 2384-2427.
- Greaves, M.J., Elderfield, H., and Sholkovitz, E.R., (1999) Aeolian sources of rare earth elements to the Western Pacific Ocean. *Mar. Chem.* 68, 31-38.
- Haley, B.A., Klinkhammer, G.P. and McManus, J. (2004), Rare earth elements in pore waters of marine sediments. *Geochim. Cosmochim. Acta*, 68, 1265-1279.
- Hallock, P. (2001) Coral reefs, carbonate sediments, nutrients, and global change. The history and sedimentology of ancient reef systems, in Stanley, G.D., New York, Kluwer Academic/Plenum Publishers. 387-427.
- Hongo, Y., Obata, H., Alibo, D.S., and Nozaki, Y. (2006) Spatial variations of Rare Earth Elements in North Pacific surface water. *J. Oceanogr.* 62, 441-455.
- Hood, A.v.S., Planavsky, N.J., Wallace, M.W. and Wang, X. (2018) The effects of diagenesis on geochemical paleoredox proxies in sedimentary carbonates. *Geochim. Cosmochim. Acta*, 232, 265-287.
- Hueter, A., Huck, S., Bodin, S., Heimhofer, U., Weyer, S., Jochum, K.P., and Immenhauser, A. (2019) Central Tethyan platform-top hypoxia during Oceanic Anoxic Event 1a: *Clim. Past*, 15, 1327-1344,
- Illing, L.V. (1954) Bahaman calcareous sands: *AAPG Bull.*, 38, 1-95.

- James, N.P. (1997) The cool-water carbonate depositional realm, in James, N.P., and Clarke, J.A.D., eds., *Cool-water Carbonates*. SEPM Special Publication, v. 56, p. 1-20.
- Lawrence, M.G., Greig, A., Collerson, K.D. and Kamber, B.S. (2006) Rare earth element and yttrium variability in southeast Queensland waterways. *Aquat. Geochem.*, 12, 39–72.
- Lees, A. (1975) Possible influence of salinity and temperature on modern shelf carbonate sedimentation. *Mar. Geol.*, 19, 159–198.
- Lees, A., and Buller, A.T. (1972) Modern temperate-water and warm-water shelf carbonate sediments contrasted. *Mar. Geol.*, 13, M67–M73.
- Li, F., Yan, J., Burne, R.V., Chen, Z.-Q., Algeo, T.J., Zhang, W., Tian, L. Gan, Y., and Xie, S. (2017) Paleo-seawater REE compositions and microbial signatures preserved in laminae of Lower Triassic ooids. *Palaeogeog. Palaeoclimatol. Palaeoecol.*, 486, 96-107.
- Liu, X.-M., Hardisty, D.S., Lyons, T.W., and Swart, P.K., (2019) Evaluating the fidelity of the cerium paleoredox tracer during variable carbonate diagenesis on the Great Bahama Bank. *Geochim. Cosmochim. Acta*, 248, 25-42.
- Logan, B.W. (1969) Carbonate Sediments and Reefs, Yucatan Shelf, Mexico. *Am. Assoc. Petr. Geol. Memoir* 11, 355.
- Lowery, J.G., and Rankey, E.C. (2017) Controls on geomorphology and sedimentology of shoreface-beach ridge-lagoon system on a low-energy carbonate ramp: Holocene, Northwestern Yucatan Shelf, Mexico: *J. Sed. Res.*, 87, 546-566.
- Lukasik, J.J., James, N.P., McGowran, B., and Bone, Y. (2000) An epeiric ramp: low-energy, cool-water carbonate facies in a Tertiary inland sea, Murray Basin, South Australia: *Sedimentol.*, 47, 851-881.
- Luo, Y.-R., and Byrne, R.H. (2004) Carbonate complexation of yttrium and the rare earth elements in natural waters. *Geochim. Cosmochim. Acta* 68, 691–699.
- Marx, S.K., Kamber, B.S., and McGowan, H.A. (2005) Provenance of long-travelled dust determined with ultra-trace-element composition: a pilot study with samples from New Zealand glaciers. *Earth Surf. Process. Landf.* 30, 699–716.
- McLennan, S.M. (1989) Rare earth elements in sedimentary rocks: influence of provenance and sedimentary processes. *Rev. Mineral.* 11, 169–200.

Merino, M. (1997) Upwelling on the Yucatan Shelf: Hydrographic evidence. *J Mar. Sys.*, 13, 101-121.

Michel, J., Laugie, M., Pohl, A., Lanteaume, C., Masse, J.-P., Donnadieu, Y., and Borgomano, J. (2019) Marine carbonate factories: A global model of carbonate platform distribution: *Int. J. Earth Sci.*, <https://doi.org/10.1007/s00531-019-01742-6>.

Michel, J., Borgomano, J., and Reijmer, J.J.G. (2018) Heterozoan carbonates: When, where and why? A synthesis on parameters controlling carbonate production and occurrences. *Earth-Sci. Rev.*, 182, 50-67.

Mutti, M., and Hallock, P., (2003) Carbonate systems along nutrient and temperature gradients: some sedimentological and geochemical constraints: *Int. J. Earth Sci. (Geol. Rundsch.)*, 92, 465-475

Neal, T. (2020) Hydrodynamic controls on sedimentology and geomorphology of marine-carbonate ramps: Insights from a Holocene analogue, northern Yucatan Shelf, Mexico. [unpub. M.S. thesis, University of Kansas], 81 p.

Nothdurft, L.D., Webb, G.E. and Kamber, B.S. (2004) Rare earth element geochemistry of Late Devonian reefal carbonates, Canning basin, Western Australia: confirmation of a seawater REE proxy in ancient limestones. *Geochim. Cosmochim. Acta*, 68, 263-283.

Nozaki, Y., Zhang, J., and Amakawa, H. (1997) The fractionation between Y and Ho in the marine environment. *Earth Plan. Sci. Let.*, 148, 329-340.

Osborne, A.H., Hathorne, E.C., Schijf, J., Plancherel, Y., Böning, P., and Frank, M. (2017) The potential of sedimentary foraminiferal rare earth element patterns to trace water masses in the past. *Geochem. Geophys. Geosyst.*, 18, 1550-1568.

Osborne, A. H., Haley, B.A., Hathorne, E.C, Plancherel, Y., and Frank, M. (2015) Rare earth element distribution in Caribbean seawater: Continental inputs versus lateral transport of distinct REE compositions in subsurface water masses. *Mar. Chem.*, 177, 172- 183.

Pattan, J.N., Pearce, N.J.G., and Mislankar, P.G. (2005) Constraints in using Cerium-anomaly of bulk sediments as an indicator of paleo bottom water redox environment: A case study from the Central Indian Ocean Basin. *Chem. Geol.*, 221, 260-278.

- Purdy, E.G. (1963) Recent calcium carbonate facies of the Great Bahama Bank. 2. Sedimentary facies. *J. Geol.*, 71, 472-497.
- Rankey, E.C., and Reeder, S.L. (2010) Controls on platform-scale patterns of surface sediments, shallow Holocene platforms, Bahamas. *Sedimentol.* 57, 1545-1565.
- Read, J.F. (1985) Carbonate platform facies models. *Am. Assoc. Petrol. Geol. Bull.*, 69, 1-21.
- Saha, N., Webb, G.E., Zhao, J.-X., Nguyen, A.D., Lewis, S.E., and Lough, J.M., 2019, Coral-based high-resolution rare earth element proxy for terrestrial sediment discharge affecting coastal seawater quality, Great Barrier Reef. *Geochim. Cosmochim. Acta*, 254, 173-191.
- Scherer, M., and Seitz, H. (1980) Rare-earth element distribution in Holocene and Pleistocene corals and their redistribution during diagenesis. *Chem. Geol.*, 28, 279-289.
- Schlager, W. (2003) Benthic carbonate factories of the Phanerozoic. *Int. J. Earth Sci.*, 92, 445-464.
- Schlager, W. (2005) Carbonate Sedimentology and Sequence Stratigraphy. *SEPM Concepts in Sedimentology and Paleontology*, 8, 200 p.
- Shinn, E.A., Lloyd, R.M., and Ginsburg, R.N. (1969) Anatomy of a modern carbonate tidal flat, Andros Island, Bahamas. *J. Sed. Petrol.*, 39, 1202-1228.
- Sholkovitz, E.R., Landing, W.M., and Lewis, B.L. (1994) Ocean particle chemistry: the fractionation of rare earth elements between suspended particles and seawater. *Geochim. Cosmochim. Acta* 58, 1567-1579.
- Tachikawa, K., Jeandel, C., Vangriesheim, A., and Dupré, B. (1999) Distribution of rare earth elements and neodymium isotopes in suspended particles of the tropical Atlantic Ocean (EUMELI site). *Deep-Sea Res. I* 46, 733-755.
- Tang, Y., Han, G., Wu, Q., and Xu, Z. (2013) Use of rare earth element patterns to trace the provenance of the atmospheric dust near Beijing, China. *Environ. Earth Sci.* 68, 871-879.
- Tostevin, R., Shields, G.A., Tarbuck, G.M., He, T., Clarkson, M.O., and Wood, R.A. (2016) Effective use of cerium anomalies as a redox proxy in carbonate-dominated marine settings. *Chem. Geol.*, 438, 146-162.

- van de Flierdt, T., *et al.* (2012), GEOTRACES intercalibration of neodymium isotopes and rare earth element concentrations in seawater and suspended particles. Part 1: Reproducibility of results for the international intercomparison. *Limnol. Oceanogr. Methods*, 10, 234– 251.
- Webb, G.E., and Kamber, B.S. (2000) Rare earth elements in Holocene reefal microbialites: A new shallow seawater proxy. *Geochim. Cosmochim. Acta*, 64, 1557-1565
- Westphal, H., Halfar, J., and Freiwald, A. (2010) Heterozoan carbonates in subtropical and tropical settings in the present and past. *Int. J. Earth Sci.*, 99, S153-S169.
- Wright, V.P., and Burchette, T.P., Eds. (1998) Carbonate ramps. *Geol. Soc., Spec. Publ.* 149.
- Xiong, Z., Li, T., Algeo, T., Chang, F., Yin, X. and Xu, Z. (2012) Rare earth element geochemistry of laminated diatom mats from tropical West Pacific: Evidence for more reducing bottomwaters and higher primary productivity during the Last Glacial Maximum. *Chem. Geol.*, 296,103-118.
- Zhang, J., and Nozaki, Y., 1996. Rare earth elements and yttrium in seawater: ICP-MS determinations in the East Caroline, Coral Sea, and South Fiji basins of the western South Pacific Ocean. *Geochim. Cosmochim. Acta*, 60, 4631-4644.
- Zheng X., Plancherel Y., Saito M. A., Scott P. and Henderson G. M. (2016) Rare earth elements (REEs) in the tropical South Atlantic and quantitative deconvolution of their non-conservative behaviour. *Geochim. Cosmochim. Acta*, 177, 217–237.
- Zhao, M.-Y, and Zheng, Y.-F. (2014) Marine carbonate records of terrigenous input into Paleotethyan seawater: Geochemical constraints from Carboniferous limestones: *Geochim. Cosmochim. Acta*, 141, 508-531.
- Zhao, M.-Y, and Zheng, Y.-F. (2017) A geochemical framework for retrieving the linked depositional and diagenetic histories of marine carbonates. *Earth Planet. Sci. Let.*, 460, 213-221.

FIGURE CAPTIONS

Figure 1. General location and setting, Yucatan Shelf, southern Gulf of Mexico. The study focuses on the north-west part of the Yucatan Peninsula [Sisal (Sis) and Celestun (Cel)], but summarizes results from other studies near Holbox (Hx) (Neal, 2020) and Isla Arena (IA) (Lowery & Rankey, 2017). Approximate location of the shelfbreak is indicated by the dashed line.

Figure 2. Representative photos of various bottom types, Sisal transects. (A) Bare sandy bioturbated bottom with an urchin, more common near the shoreline. Water depth is *ca* 5 m. (B) Bare gravel bottom, consisting mostly of bivalve fragments, at *ca* 6 m depth. (C) Vegetated bottom at *ca* 6 m depth, with calcareous green algae and brown algae. (D) Rocky bottom at water depth *ca* 7 m. Diver's tank is *ca* 0.75 m tall. (E) Rippled sand to gravel with scattered fleshy algal cover, from >40 km offshore in water depth *ca* 25 m. (F) Abundant fleshy algal cover, common during summer months. Coral in foreground is *Solenastrea hyades*, a species adapted to cooler and turbid water. Water depth is *ca* 26 m.

Figure 3. Representative photographs of various bottom types, Celestun transects. (A) Bare sand with abundant bivalves and echinoderm, a bottom type common nearshore. Water depth *ca* 3 m. (B) Bioturbated seagrass meadow in water depth *ca* 3 m. (C) *Halimeda*-seagrass covered bottom at water depth *ca* 6 m. (D) Bare sandy bottom from the zone with the subaqueous dunes, here in water depth of *ca* 9 m. (E) Two of the coral species that occur in the area, *Oculina varicosa* and *Cladocora arbuscula*. Water depth *ca* 6 m (F) Encrusting *Cliona* sponge, over an unknown coral boulder and limestone, from water depth *ca* 7 m.

Figure 4. Bottom types and sediment size attributes. (A) Bottom type, Sisal. (B) Bottom type, Celestun. Note the common vegetated bottoms, offshore Celestun, and the more widespread rocky bottoms, offshore Sisal. (C) Grain sizes, Sisal. (D) Grain sizes, Celestun. The data – bars expressed as a percentage of each grain size fraction – suggest general offshore decrease in abundance of the fine fraction, but otherwise considerable variability is present.

Figure 5. Representative thin-section photomicrographs, Sisal (A) to (C) and Celestun (D) to (F). (A) Moderately well-sorted fine to medium sand, such as that common within several 100 m of shore. (B) Poorly sorted fine sand to gravel from a bare sand bottom. Note the diverse skeletal association and the lithoclasts (yellow arrows). (C) Moderately sorted medium sand to gravel, including bored ooids, some of which are highlighted by yellow arrows. (D) Moderately well-sorted fine to medium sand, including bivalves, foraminifera, and fine, rounded to angular skeletal fragments. (E) Medium sand to gravel, including coarse bivalve fragments, many of which are intensively bored (see the yellow arrow) and foraminifera, with some *Halimeda* fragments. (F) Moderately well-sorted fine to medium sand, from near the crest of an offshore subaqueous dune.

Figure 6. Paired remote-sensing image (A) and cartoon bottom-type map (B) of the north-west Yucatan Peninsula focus areas. Note the greater width of nearshore belts with bare sediment, vegetation-dominated, and sandy bottom with linear bars offshore of Celestun, relative to those off of Sisal. Similarly, areas farther offshore from those belts include sandy to rocky bottom and linear sand bars off of Sisal, but much more complex barforms off of Celestun.

Figure 7. Regional long-term salinity and temperature trends. (A) Mean salinity, November 2017. The Yucatan Shelf north of the peninsula has slightly elevated salinity, and salinity increases to the west. (B) Mean salinity, May 2018. Note the similar patterns, but slightly higher mean salinities on the shelf and into the Bay of Campeche. Data for parts (A) and (B) from Naval Research Laboratory Gulf of Mexico HYCOM (<https://www7320.nrlssc.navy.mil/hycomGOM2/skill.html>). (C) Mean sea-surface temperature, November 2017. The data illustrate the warm waters of the Caribbean extending into the Gulf of Mexico as the Loop Current ('LC'), but the presence of cooler water of the shelf just north of the Yucatan Peninsula. (D) Mean sea-surface temperature, May 2018, illustrating markedly cooler water near the north shelf of the Yucatan Peninsula. (E) Mean chlorophyll-a, November 2017; (F) Mean chlorophyll-a, May 2018. Note that elevated values are common

regionally during the winter months (E) but are focused more nearshore in the summer months (F). Data in (C) to (F) are courtesy of NOAA, Environmental Research Division (<https://coastwatch.pfeg.noaa.gov/>).

Figure 8. Chemical oceanographic change through time, derived from *in situ* sensors, offshore Sisal. The left column shows data during spring (12 April to 21 May 2018), the right column includes data from early summer (29 May to 22 June 2018). Data include nearshore (blue) and offshore (orange) sensors. (A) and (B) Temperature; (C) and (D) salinity; (E) and (F) total suspended solids; (G) and (H) dissolved oxygen. See text for discussion.

Figure 9. Matrix of changes in optical properties (left column), sea-surface temperature (middle column), and Chlorophyll-a (right column) for illustrative days demonstrate the spatial and temporal oceanographic changes. Individual dates, and comparisons among dates, inform interpretations of the changes. (A) to (C) 9 April, 2018, a representative spring day with warmer (>27°C) water only in nearshore regions of the western shelf; (D) to (F) 18 April 2018, just after passage of a Norte. Note the elevated suspended sediment, higher Chlorophyll-a, and cooler temperatures, relative to 9 April; (G) to (I) 10 June 2018. Data show a representative summer day with cooler, upwelled water on the shallow shelf, north of the peninsula; (J) to (L) 22 June 2018. A succession of cloudy days kept water temperatures low, but upwelling appears to have continued, suggested by the especially low temperatures and increased Chlorophyll-a, especially notable on the eastern shelf, near Holbox.; (M) to (O) 31 January 2019. Data are a representative winter day, with abundant sediment, elevated Chl-a, and cool water temperatures (below 24°C). Data are from <https://worldview.earthdata.nasa.gov/>.

Figure 10. Maps of the Sisal and Celestun areas, showing: (A) abundance of SiO₂, all samples; (B) abundance of Al₂O₃, all samples; (C) abundance of Th, all samples; (D) PAAS-normalized REEs from sediment with Al₂O₃ less than or equal to 0.1%, colour coded by area. (E) Means of PAAS-normalized REEs data of part (D) for each area. Note the elevated REE near Holbox. See text for detailed discussion.

Figure 11. Spatial trends in REE character for samples with less than 0.1% Al₂O₃, and comparison with representative oceanographic data. The dashed curve is simply a reference for comparison among images. (A) Plot of HREE/LREE ratio on basemap of Chlorophyll-a for 3 June 2018. Note that the data include lower ratios offshore Celestun and nearshore Sisal, in areas with elevated Chlorophyll-a. Offshore Sisal (more than 15 km offshore) samples have elevated HREE/LREE ratios and generally lower Chlorophyll-a. (B) Plot of HREE/LREE ratio on a basemap of SST for 11 June 2018. Note that the area with cooler temperatures includes the more elevated ratios. (C) Plot of HREE/LREE ratio of Holbox transect. Note that data indicate ratios are more consistent, and greater than nearshore Sisal and Celestun – parts (A) and (B). (D) Plot of spatial changes in Cerium anomaly (Ce/Ce*) near Sisal and Celestun. Considerable variability is evident.

Figure 12. Relations among various REE+Y and other trace elements. Different dot colours represent different study areas in parts (A) to (E). (A) Plot of Σ REE and Nd/Yb. Only data with Yb, Nd four times the detection limit and less than 0.1% Al₂O₃ are shown. (B) Lanthanum anomaly diagram, viewed by plotting Ce anomaly versus Pr anomaly. Only data with Yb, Nd, Ce four times the detection limit and less than 0.1% Al₂O₃ are shown. (C) Plot of Y/Ho versus Nb/Yb. Only data with Yb, Nd, Ho, and Y four times the detection limit and less than 0.1% Al₂O₃ are shown. (D) and (E) Cross-plot of Al₂O₃ (D) and thorium (E) versus Y/Ho; all data are shown. Note that there are no evident relations between Al₂O₃ or Th and Y/Ho, or among areas. (F) Plot of Al₂O₃ versus SiO₂, colour coded by Y/Ho. See text for discussion.

Figure 13. Cross-plot of stable oxygen and carbon isotope values for Yucatan samples. Each data point is colour coded by sampling location. Note that Holbox samples include the highest $\delta^{18}\text{O}$ and $\delta^{13}\text{C}$ values.

Figure 14. (A) Conceptual model for the distribution of zones of chemically distinct water masses. Water mass zones have diffuse boundaries. Coloured rectangles represent

approximate areas from which data in parts (B) and (C) are extracted. See text for discussion. (B) Seasonal changes in Chlorophyll-a, illustrated by plot of average Chlorophyll-a for May 2018 versus average Chlorophyll-a for November 2018. Note the distinct patterns among zones, with values greatest in Zone 1, lowest in Zone 3. Not also that November Chlorophyll-a is higher in all zones. (C) Seasonal changes in SST, documented by plot of average SST for May 2018 versus average SST in November 2017. Zone 1, which lies in shallower water, shows more variability and considerably warmer water in the summer months. Zone 2 shows the opposite trend, with cooler water in summer. See text for discussion.

Figure 15. (A) General interpretive diagram of patterns off the coast of the north Yucatan Peninsula off of Sisal. Across the shoreface, several water masses occur; these water masses have distinct chemical oceanographic and sedimentologic attributes. (B) Schematic plot of a complete stratigraphic succession that could form with shoreface progradation of a system comparable to that illustrated in part (A). A shallowing-upward facies succession would exhibit changes in faunal association, Ce anomaly, and HREE/LREE ratios. See text for discussion.

Table 1. Rare-earth element (REE) concentrations, subdivided by area. Recall that these data are the PAAS (Post-Archean Australian Shale) normalized values.

Table 1

	Holbox	Sisal	Celestun	Isla Arena
<i>Mean REE Conc. (ppm)</i>	0.66	0.52	0.52	0.49
<i>Minimum</i>	0.30	0.18	0.37	0.19
<i>Maximum</i>	0.83	1.08	0.69	0.81

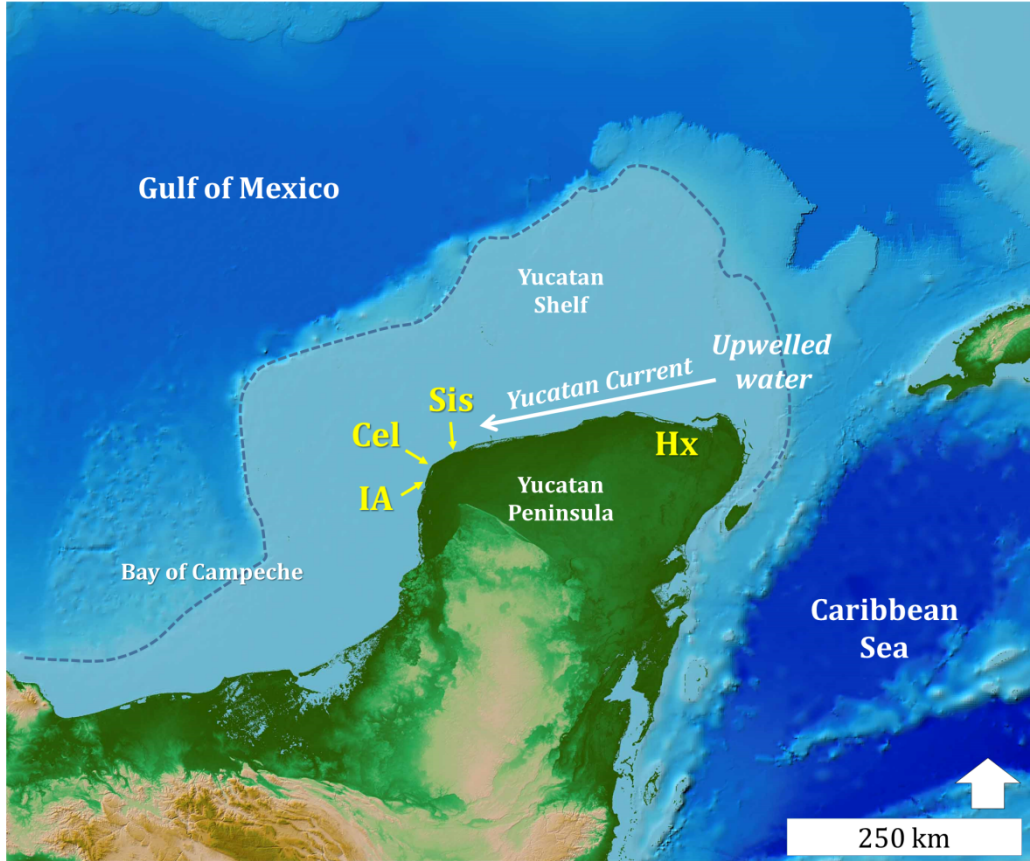


Figure 1

sed_12780_f1.tif

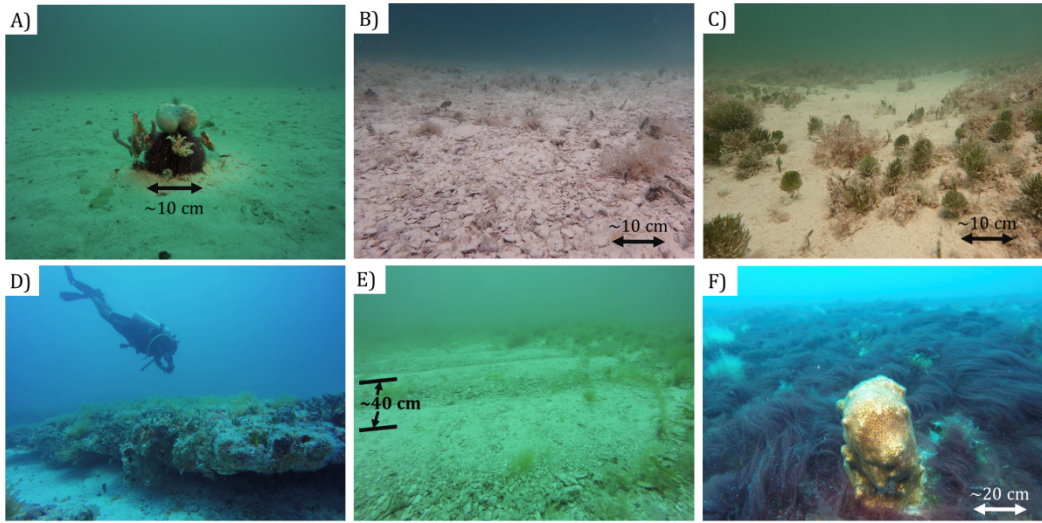


Figure 2

sed_12780_f2.tif

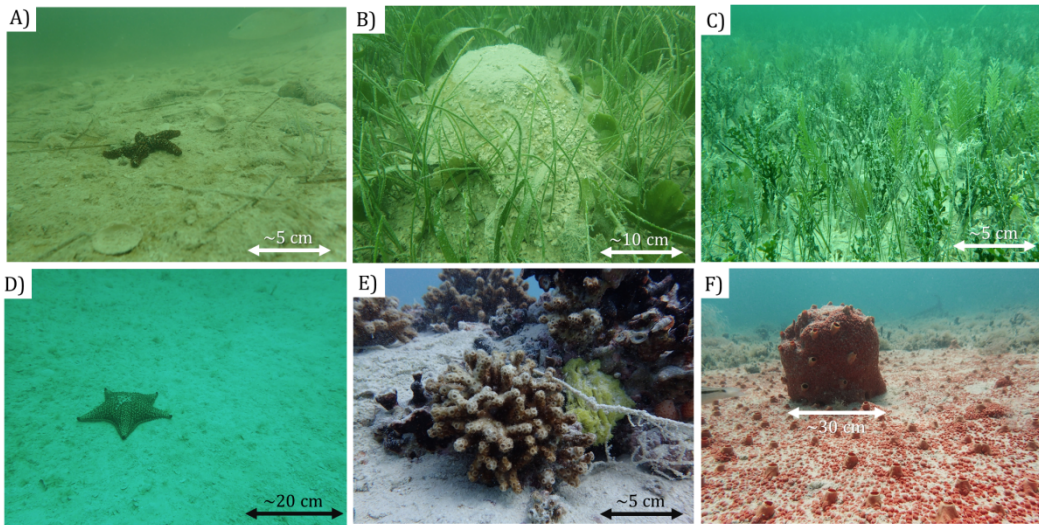


Figure 3

sed_12780_f3.tif

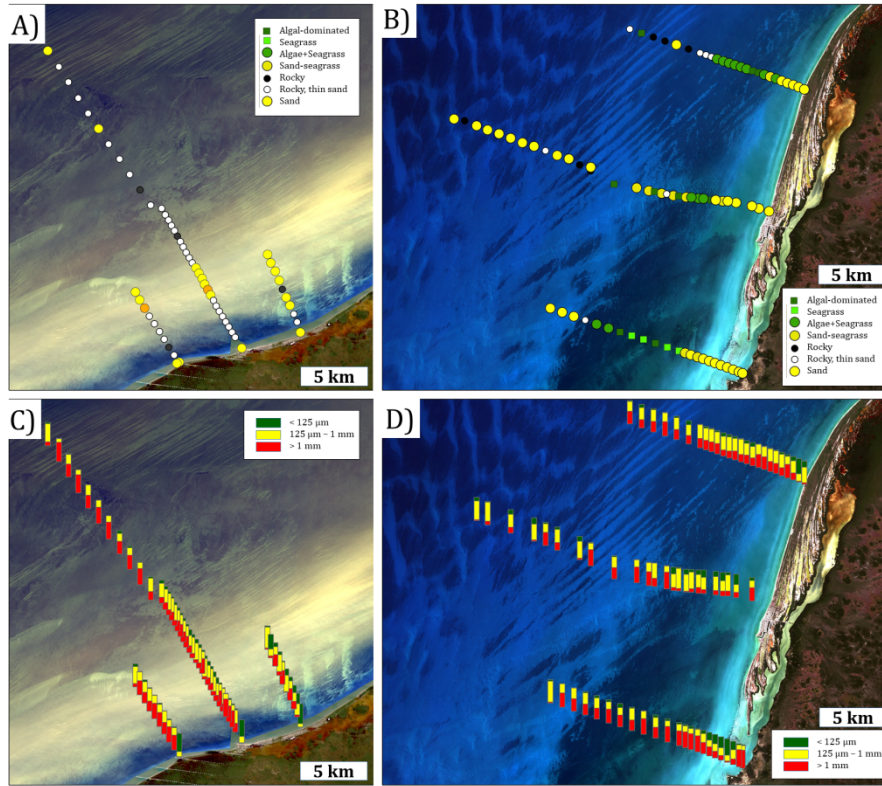


Figure 4

sed_12780_f4.tif

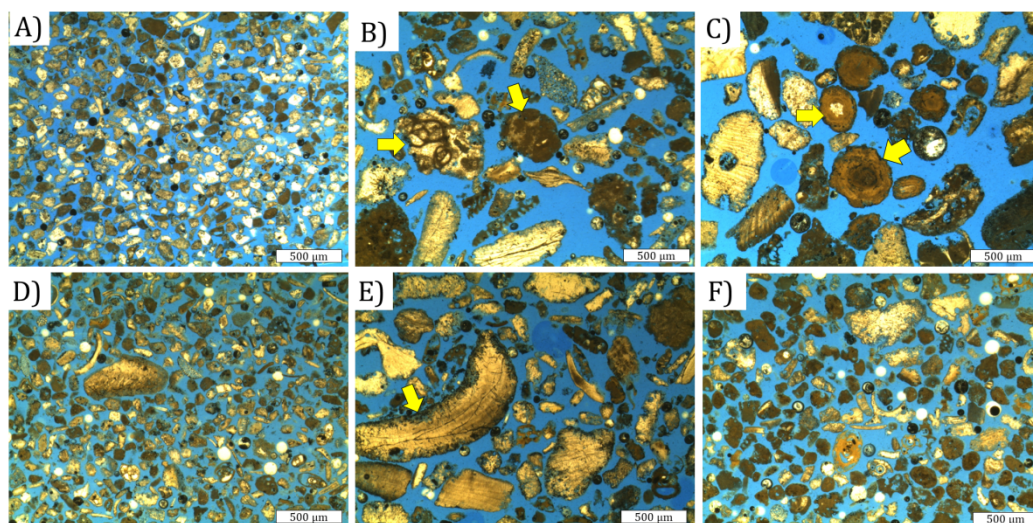


Figure 5

sed_12780_f5.tif

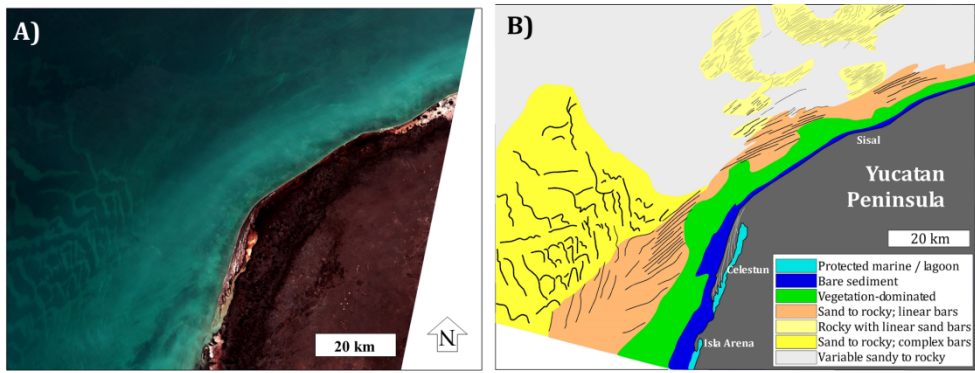


Figure 6

sed_12780_f6.tif

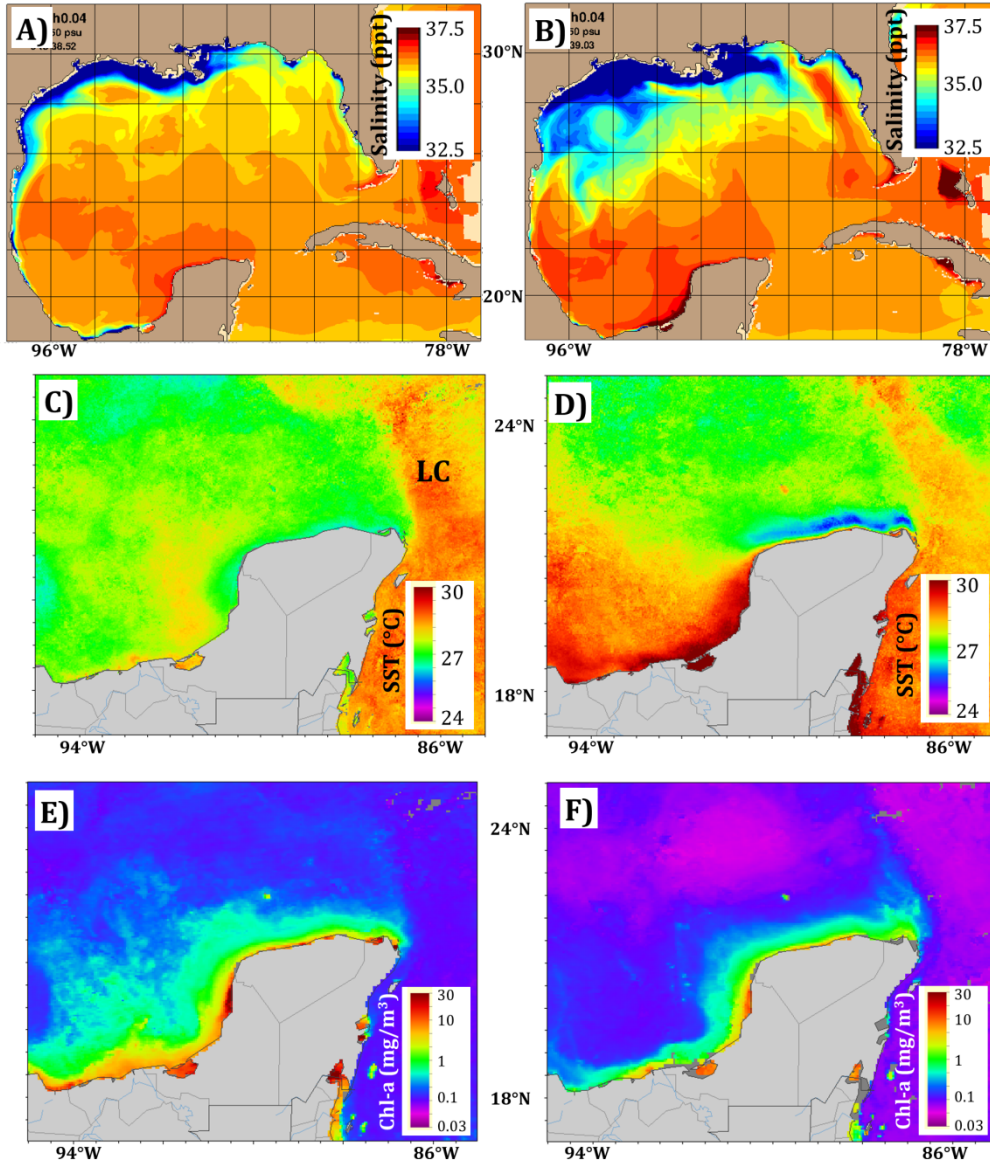


Figure 7

sed_12780_f7.tif

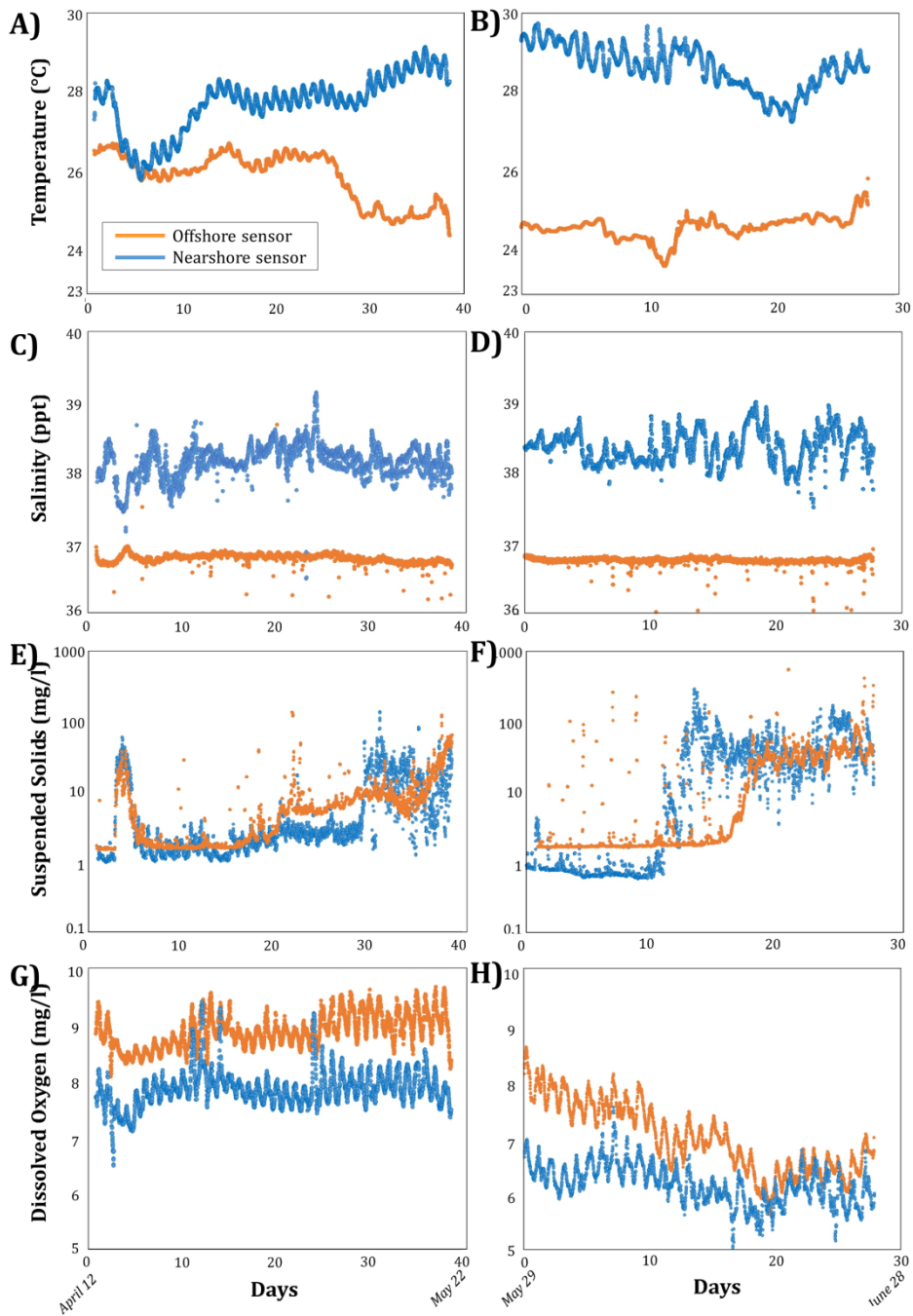


Figure 8

sed_12780_f8.tif

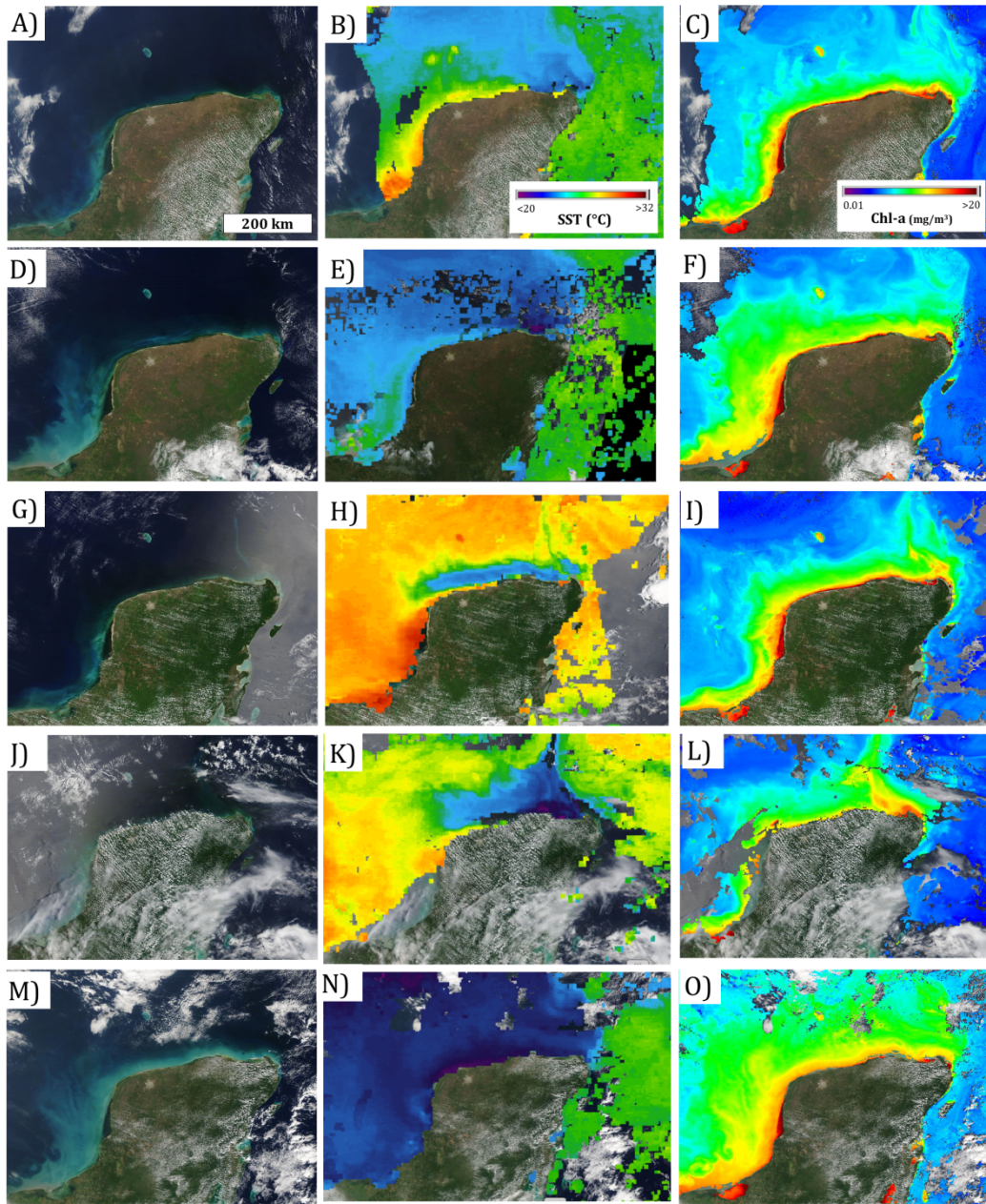


Figure 9

sed_12780_f9.tif

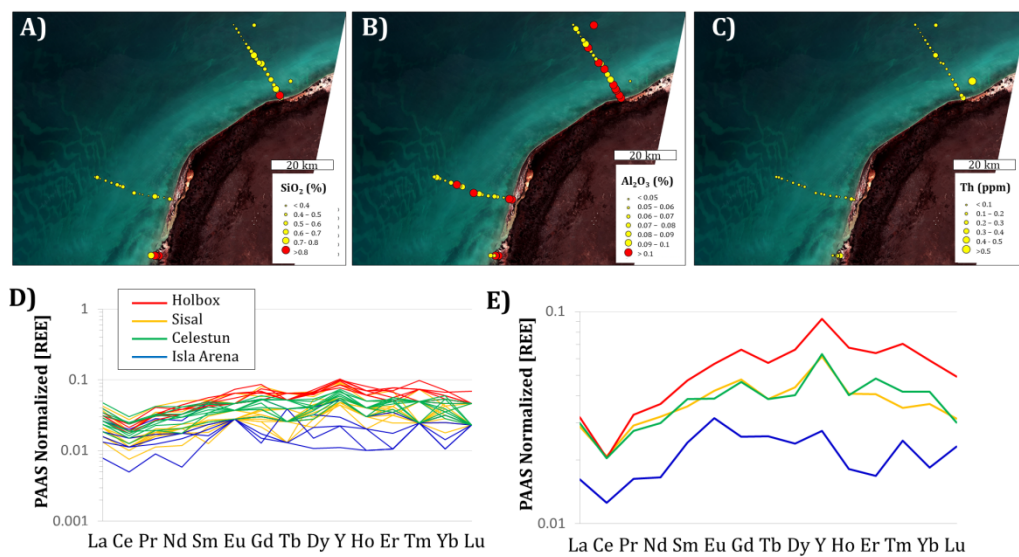


Figure 10

sed_12780_f10.tif

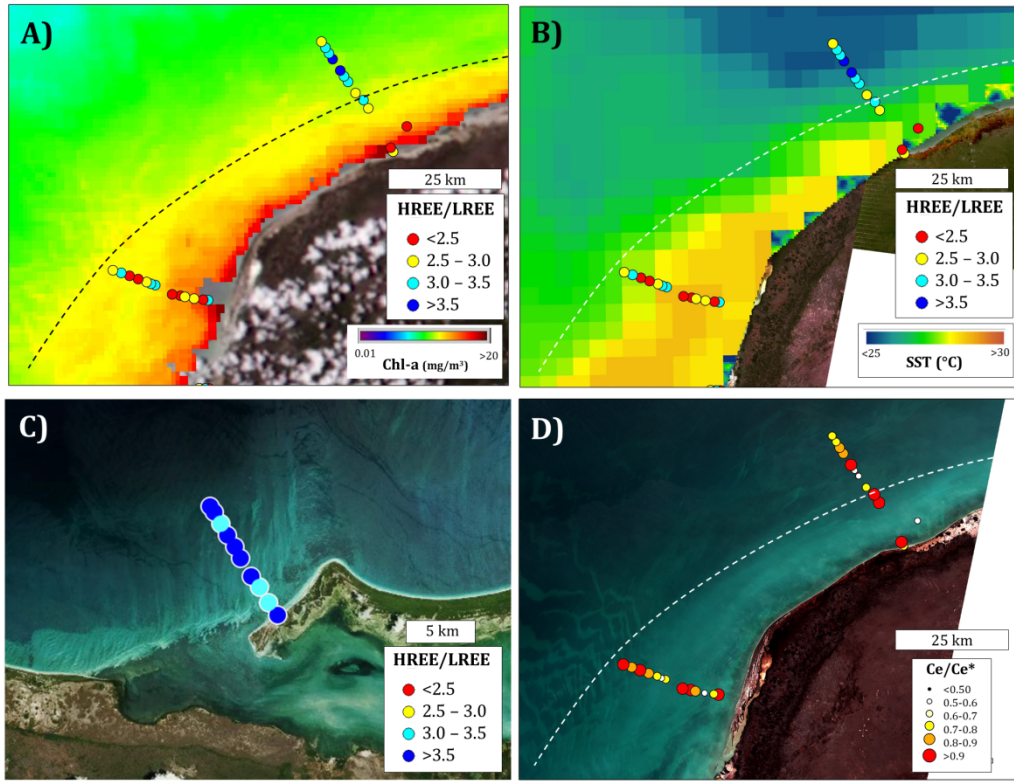


Figure 11

sed_12780_f11.tif

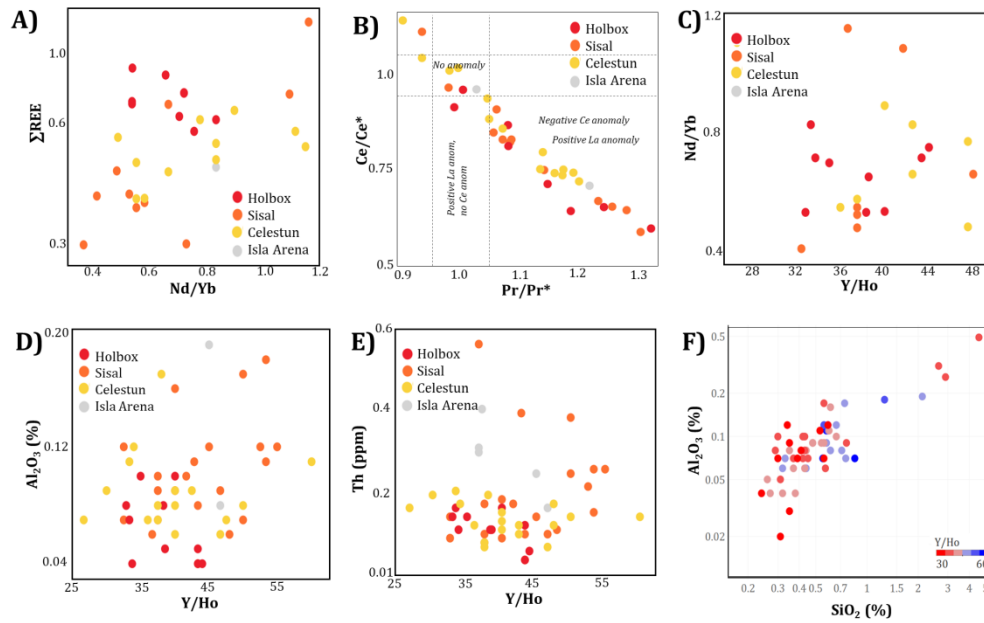


Figure 12

sed_12780_f12.tif

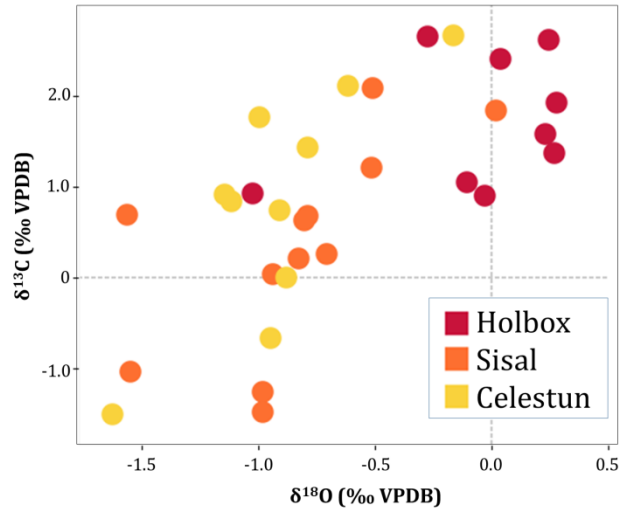


Figure 13

sed_12780_f13.tif

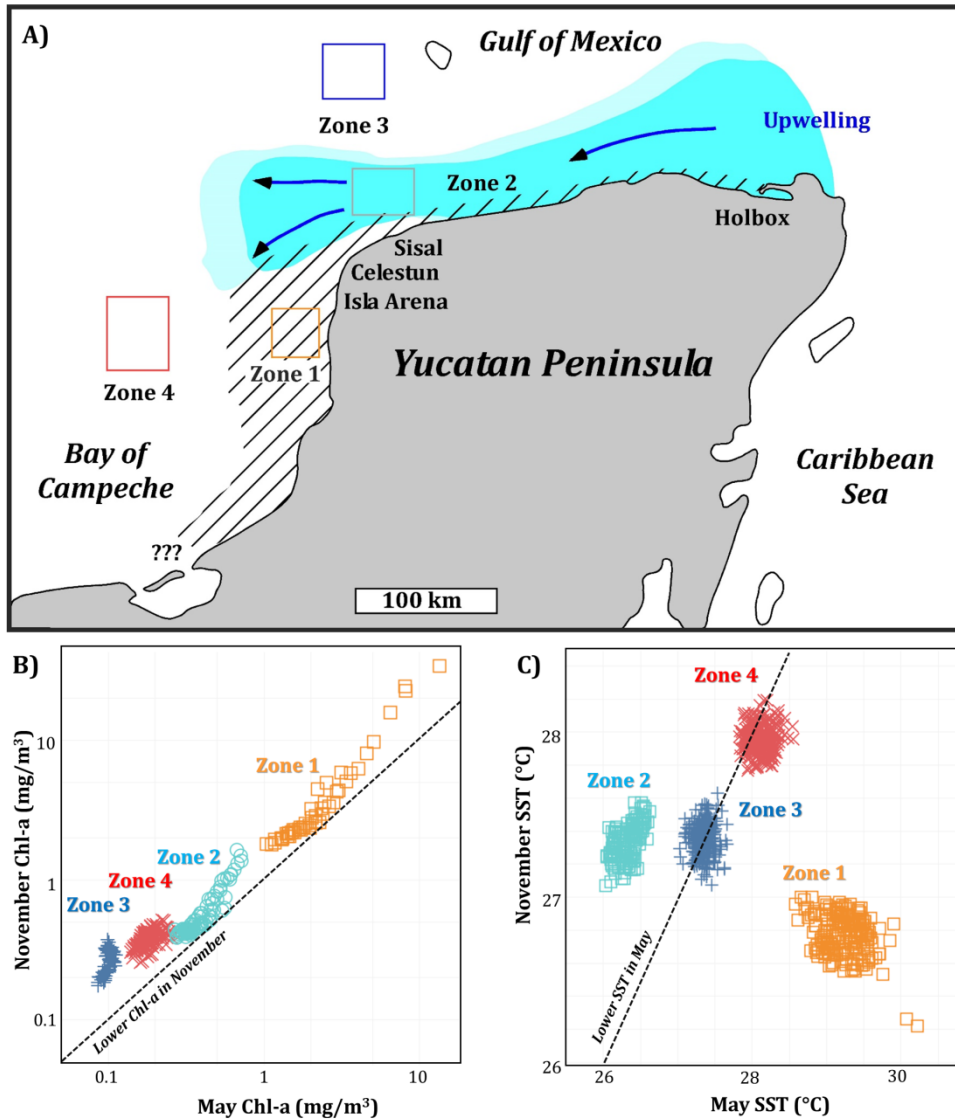
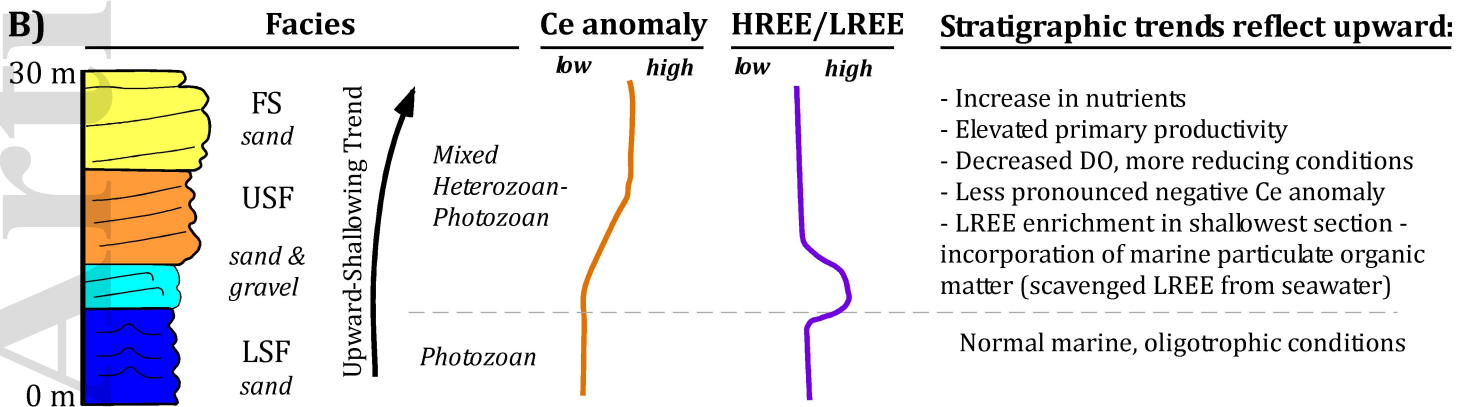
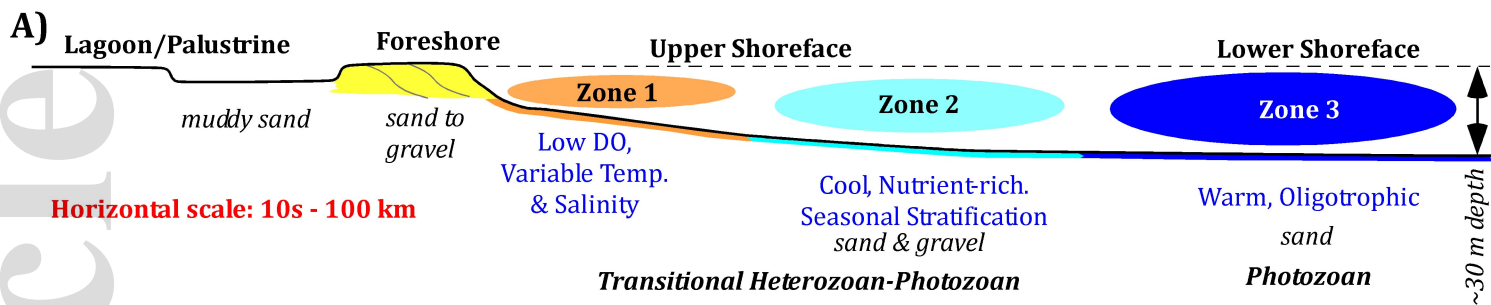


Figure 14

sed_12780_f14.tif



sed_12780_f15.jpg